2000

The effects of gasdynamics, cooling, star formation, and numerical resolution in simulations of cluster formation

GF Lewis

A Babul

N Katz
University of Massachusetts - Amherst

T Quinn

L Hernquist

See next page for additional authors

The Effects of Gas Dynamics, Cooling, Star Formation, and Numerical Resolution in Simulations of Cluster Formation

Geraint F. Lewis[1], Arif Babul[2], Neal Katz[3], Thomas Quinn[4], Lars Hernquist[5] & David H. Weinberg[6]

Received _____; accepted _____

[1]Fellow of the Pacific Institute of Mathematical Sciences 1998-1999,

Dept. of Physics and Astronomy, University of Victoria, PO Box 3055, Victoria, B.C., V8W 3P6, Canada

& Astronomy Dept., University of Washington, Box 351580, Seattle WA 98195-1580, U.S.A.

Electronic mail: gfl@astro.washington.edu

Electronic mail: gfl@uvastro.phys.uvic.ca

[2]Dept. of Physics and Astronomy, University of Victoria, PO Box 3055, Victoria, B.C., V8W 3P6, Canada

Electronic mail: babul@uvic.ca

[3]Dept. of Physics and Astronomy, University of Massachusetts, Amherst, MA 01003, U.S.A.

Electronic mail: nsk@kaka.phast.umass.edu

[4]Astronomy Dept., University of Washington, Box 351580, Seattle WA 98195-1580, U.S.A.

Electronic mail: trq@astro.washington.edu

[5]Department of Astronomy, Harvard University, 60 Garden Street, Cambridge MA 02138

Electronic mail: lars@cfa.harvard.edu

[6]Dept. of Astronomy, The Ohio State University, Columbus, OH 43210, U.S.A.

Electronic mail: dhw@astronomy.ohio-state.edu

Submitted to the Astrophysical Journal

ABSTRACT

We present the analysis of a suite of simulations of a Virgo mass galaxy cluster. Undertaken within the framework of standard cold dark matter cosmology, these simulations were performed at differing resolutions and with increasingly complex physical processes, with the goal of identifying the effects of each on the evolution of the cluster. We focus on the cluster at the present epoch and examine properties including the radial distributions of density, temperature, entropy and velocity. We also map 'observable' projected properties such as the surface mass density, X-ray surface brightness and Sunyaev-Zel'dovich signature. We identify significant differences between the simulations, which highlights the need for caution when comparing numerical simulations to observations of galaxy clusters. While resolution affects the inner density profile in dark matter simulations, the addition of a gaseous component, especially one that cools and forms stars, affects the entire cluster. For example, in simulations with gas dynamics but no cooling, improving the gravitational force resolution from 200 kpc to 14 kpc increases the X-ray luminosity and emission-weighted temperature by factors of 2.9 and 1.6, respectively, and it changes the form of the X-ray surface brightness and temperature profiles. At the higher resolution, a simulation that includes cooling and star formation converts 30% of the cluster baryons into stars and produces a massive central galaxy that substantially alters the cluster potential well. This cluster has 20% higher X-ray luminosity and 30% higher emission-weighted temperature than the corresponding cluster in the no-cooling simulation. Its properties are reasonably close to those of observed XD clusters, with conversion of cooled gas into stars greatly reducing the observational conflicts found by Suginohara & Ostriker in simulations with cooling but no star formation. We conclude that both resolution and included physical processes

play an important role in simulating the formation and evolution of galaxy clusters. Therefore, physical inferences drawn from simulations that do not include a gaseous component that can cool and form stars present a poor representation of reality.

Subject headings: Galaxy Clusters; Numerical Simulations; Star Formation

1. Introduction

With masses exceeding $10^{13}\,M_{\odot}$, clusters of galaxies represent the largest gravitationally bound objects in the Universe. For a number of decades, these systems have been the focus of intense observational and theoretical study in an effort to understand the evolving inter-relationships between the hot diffuse intracluster gas, the galaxies, and the inferred dark matter component that make up the clusters. In recent years, rapid advances in computer technology and available computational power, coupled with the development of increasingly sophisticated numerical simulation codes, have offered the possibility of studying the formation and evolution of cosmological structures like clusters in unprecedented detail.

The developmental history of the increase in resolution and physical complexity of the numerical simulations has closely followed the growth of computational power. Early efforts considered simple systems consisting only of dark matter (e.g. Peebles 1970); the evolution of such systems depends solely on the action of gravity. Since the number of particles involved was relatively small, the gravitational forces were calculated directly. To enhance the degree of realism, novel techniques (such as particle-mesh and tree-codes) were developed so that simulations with an increasingly larger number of particles would be computationally feasible.

More recent simulations have also included a baryonic component. This was made possible using techniques like smoothed particle hydrodynamics (SPH), to study jointly the distributions of gas and dark matter within the cluster environment. Unlike the dark matter, the evolution of this baryonic material depends not only on gravity but also on processes such as cooling via radiative and Compton processes, heating via shocks and the deposition of energy by supernova explosions, the conversion of gas into stars, etc. Even in simulations where the baryonic component is treated as a simple adiabatic fluid, one still needs to consider the impact of processes like compressional and shock heating. Such heating modifies the subsequent motions of baryonic material within the cluster potential. The effects of these non-gravitational processes can be complex, and they can interact in unexpected ways with the effects of finite numerical resolution. The physics of star formation and supernova feedback is poorly understood; one can introduce plausible "recipes" for converting cooled gas into stars, but until these recipes are better constrained by observations they remain a source of uncertainty in numerical calculations.

How much do the details of the resultant simulated clusters depend on the characteristics of the simulation? Specifically, how do properties such as the mass and force resolution and the degree to which non-gravitational physical processes are included affect the results? In this paper we address these questions by considering a family of simulations modeling the formation of a Virgo-sized cluster evolved with differing resolutions and including different physical processes. A complementary study was recently presented by Bryan and Norman (1998); while they considered a sample of clusters, their simulations were undertaken at lower resolution and did not include the cooling of gas and subsequent star formation.

In §2 we briefly review the results from recent simulations. In §3 we describe our methods. The three-dimensional radial profiles of a number of physical properties of the simulated clusters are compared in §4, more specifically the total and dark matter

distributions in §4.1, the circular velocity in §4.2, the gas density profile and baryon fraction in §4.3, the cooling timescales in §4.4, the gas temperature distribution in §4.5 and the entropy in §4.6. Projected, two-dimensional distributions, akin to observable properties of galaxy cluster, are presented in §5. These are the total and dark matter distributions in §5.1, X-ray surface brightness in §5.2, X-ray temperature distributions in §5.3 and the Sunyaev-Zel'dovich effect in §5.4. We discuss the implications of this study in §6, with §6.1 focusing of the effect of resolution, §6.2 on the addition of a hydrodynamic component and §6.3 the effect of allowing the gas to cool and and form stars. The conclusions of our study are presented in §7.

2. Past Simulations

Many simulations of cluster formation have been undertaken over the last three decades. While the earliest had only a dark matter component, many have included a gas component and, in more recent work, have incorporated the physics of cooling and star formation within the gaseous environment. To exhaustively summarize the details of all the previous simulations is beyond the scope of this paper. For comparison purposes, however, we present the details of a representative sample of recent cluster formation simulations in Table 1. In addition to the physical details of the simulations, such as the final cluster mass and whether or not the gas was allowed to cool and form stars, we also present the resolution limits of the various components. This includes the spatial resolution, which we define to be twice the gravitational softening length, and the dark matter and gas mass resolution, which we define to be 32 times the mass of the corresponding particle. Wherever possible we convert the gravitational softening length into its equivalent Plummer softening value. Most simulations have a spatial resolution that is constant in comoving coordinates. We append a "p" to those that have a resolution constant in physical coordinates. For

the Eulerian simulations we quote the gas mass resolution at the mean density. The gas mass resolution for a virialized object is the number in parentheses. We also define a virial mass limit to be the mass of a virialized object, an object with a mean overdensity greater than 178, that has a radius that is twice the spatial resolution scale. This should be the minimum resolvable mass of a collapsed object. All values are at $z = 0$. As one can see from this table, the various resolutions used span several orders of magnitude.

As noted in Suginohara & Ostriker (1998), these various methods reproduce the generic features of observed galaxy clusters, such as their core radii, suggesting that the overall picture of clusters forming from gravitationally driven merging and collapse of subcomponents provides a reasonable description for structure formation. While we consider this encouraging, we also feel that, owing to various numerical effects and the exclusion of various known physical components and processes, these simulations probably do not provide a complete description of the formation and evolution of galaxy clusters.

It has been argued that cooling should be important only on scales smaller than the cooling radius; gas within the cooling radius can cool within a Hubble time, leaving gas outside the cooling radius unaffected. However, the loss of central pressure support owing to this cooling will influence the hydrodynamic evolution of the entire cluster and cooling during the early stages of cluster formation can remove gas from the eventual intracluster medium by converting it into stars. For galaxy clusters the cooling radius ranges from 100 to 200 kpc depending on the size of the cluster. As we show below, cooling can greatly affect some physical properties of the cluster all the way out to the virial radius.

Similarly, one might expect the limited spatial resolution to affect only scales smaller than the spatial resolutions listed in Table 1. Since most of the cluster simulations resolve the scales of observed cluster cores, one might perhaps conclude that all the simulations have sufficient resolution. Although this may be true for the total mass density distribution,

finite resolution effects modulate the potential out to several times the spatial resolution scale. Further, since clusters form hierarchically, one might expect that it is also necessary to resolve the subunits that eventually merge to form the cluster and that not resolving the subunits will influence even larger scales (the relevant comparable resolution is the fraction of the virial radius). As we will show, some physical quantities are affected on larger scales than those listed in Table 1, sometimes approaching the virial radius.

Judging by Table 1, the mass resolutions all seem adequate to resolve galaxy clusters. But once again, it may be necessary to resolve the substructures that merge to form the galaxy clusters. Most of the simulations appear to have mass resolutions sufficient to resolve several levels down the hierarchy. When cooling is included, however, it may be necessary to resolve galactic scales.

3. Methods and Models

For the study presented here, most of the simulations were performed with TreeSPH [Hernquist & Katz (1989), hereafter HK; Katz et al. (1996), hereafter KWH], a code that unites smoothed particle hydrodynamics [SPH; Lucy (1977); Gingold & Monaghan (1977)] with the hierarchical tree method for computing gravitational forces (Barnes & Hut 1986; Hernquist 1987). Dark matter, stars, and gas are all represented by particles; collisionless material is influenced only by gravity, while gas is subject to gravitational forces, pressure gradients, and shocks. Because it uses a Lagrangian hydrodynamics algorithm and individual particle time steps, TreeSPH can perform simulations with the enormous dynamic range needed to study galaxy formation in a cosmological context. In SPH, gas properties are computed by averaging or "smoothing" over a fixed number of neighboring particles; 32 in the calculations here. When matter is distributed homogeneously, all particles have similar smoothing volumes. However, smoothing lengths in TreeSPH are

allowed to decrease in collapsing regions, in proportion to the interparticle separation, thus increasing the spatial resolution in precisely those regions where a high dynamic range is needed. In underdense regions, the smoothing lengths are larger, but this is physically reasonable because the gas distribution *is* smoother in these regions, requiring fewer particles for an accurate representation. To enable it to perform cosmological simulations TreeSPH includes periodic boundary conditions, comoving coordinates, radiative cooling, and an algorithm for star formation that turns cold, dense gas into collisionless particles and returns supernova feedback energy to the surrounding medium.

To maintain accuracy in the tree force calculation we use an opening angle criterion of of $\theta = 0.7$ (Hernquist & Katz 1989). We use a spline kernel for the gravitational force softening; this has an advantage over other forms for the softening (e.g. Plummer); forces become exactly Newtonian beyond twice the softening length. TreeSPH allows particles to have individual time steps according to their physical state, so that the pace of the overall computation is not driven by the small fraction of particles requiring the smallest time steps. To ensure accurate integrations we use the timestep criteria described in Quinn et al. (1998) and KWH for each particle with a Courant factor of 0.3 and $\epsilon_{grav} = 0.4$. To increase efficiency, we never allow the gas smoothing length to drop below 1/4 times the gravitational softening length. In the hydrodynamical calculations described here, the largest allowed timestep is 6.5×10^6 years. The smallest timestep was 32 times smaller, or 2.03×10^5 years.

To accurately simulate the formation of a galaxy cluster it is important to follow the evolution of the gravitational tidal field out to a large radius, while retaining high resolution in regions that eventually constitute the cluster. The global tidal field can affect the evolution of matter flowing into the cluster. To accomplish these goals using a minimum number of particles, hence making the problem computationally tractable, we use the

following procedure.

First, we used a Gelb & Bertschinger (1994) simulation of a large, uniform, periodic volume to create a catalog of galaxy clusters for further study. The simulation tracked the evolution of 144^3 dark matter particles within a periodic cube 100 Mpc ($H_0 = 50\,\mathrm{km\,s^{-1}\,Mpc^{-1}}$; $h = 0.5$ throughout this paper) on a side in a flat Einstein-de Sitter ($\Omega = 1$) universe. The mass of each dark matter particle in the simulation is $M_{dp} = 2.3 \times 10^{10}\,M_\odot$. The dark matter particles were imprinted with perturbations described by the standard CDM power spectrum, and evolved to the present using a P^3M algorithm (Gelb 1992) with a timestep of 1.9×10^7 years and a (Plummer) gravitational softening length of $32.5h^{-1}$ comoving kpc. The amplitude of the initial perturbations is such that the square root of the variance in $8h^{-1}$ Mpc spheres (σ_8) is 0.7 when linearly extrapolated to $z = 0$. We selected one cluster, a relatively isolated system with a circular velocity of about $1000\,\mathrm{km\,s^{-1}}$, representative of a candidate Virgo-like cluster, for more detailed study employing a hierarchical mass grid for higher resolution (Katz & White 1993).

The Gelb & Bertschinger (1994) simulation is used to identify the particles that constitute the final cluster at the present day. The new simulation volume is centered on the eventual position of the cluster. The mass resolution in the finest hierarchical grid, a spherical region of radius 20 Mpc about the center of the simulation volume, is the same as that in the original simulation (i.e. $M_{dp} = 2.3 \times 10^{10}\,M_\odot$), but it becomes successively coarser at larger distances from the cluster center. In this way, only 117,000 particles (100,000 in the central region and 17,000 outside) are needed to model the entire 100 Mpc cube, compared to over 3,000,000 if it were modeled at uniform resolution. We use the same realization of the power spectrum as before and evolve to the present using TreeSPH (no gas component) with a gravitational softening length of $35h^{-1}$ comoving kpc (equivalent

Plummer softening) and a maximum timestep of 5.2 $\times 10^7$ years. We use this simulation to initialize the final set of five simulations where the highest resolution regions are limited to only those containing particles that fall within the virial radius of the cluster at $z = 0$ and their nearest neighbors. The details of these simulations are presented below and a summary of their resolution properties is presented in Table 2.

The first of the five final simulations was a pure dark matter simulation, rerun with the same mass resolution in the high resolution regions as in the previous cases but with a gravitational softening length of $7h^{-1}$ comoving kpc (equivalent Plummer), a factor of five improvement in the spatial resolution. This simulation hereafter will be referred to as *Dark*. The total number of particles in this simulation is 68,000 with 44,000 high resolution particles and 24,000 particles of greater mass.

We perform three further simulations at the same mass resolution as *Dark* but with the addition of a hydrodynamical gas component in the high resolution regions. Of these, two had the same gravitational force resolution and hence the same spatial resolution as *Dark* and the third had a gravitational softening length of $100h^{-1}$ comoving kpc (equivalent Plummer). Since we restrict the gas smoothing length to be greater than 1/4 the gravitational softening length, this also has the effect of artificially reducing the spatial resolution of the gas. This low resolution SPH simulation and one of the two high resolution SPH simulations are evolved without supernova heating, radiative or Compton cooling, or star formation. We will refer to these two simulations as *Lowres* and *Adiabatic*, respectively. By comparing the results of these two simulations, we expect to assess the effects of spatial resolution. Note that we conform to the conventional misuse of terminology in this field by equating "non-radiative" gas dynamics with "adiabatic" gas dynamics, even though the gas in our adiabatic simulation is subject to shock heating and therefore does not evolve isentropically.

In the other high resolution hydrodynamic simulation (*Cool+SF*), the gas is allowed to undergo cooling via a number of mechanisms, including collisional excitation and ionization, recombination, free-free emission and inverse Compton cooling off the microwave background. Cooling allows the gas to collapse, where possible, into cold, dense knots. In "real" systems, gas in such knots would form stars. Unlike gas, a stellar component is collisionless and hence behaves very differently during collisions and mergers. Additionally, stars can inject energy into the surrounding medium via winds and supernova explosions. The fraction of the baryonic component locked up in stars can affect both the subsequent dynamical and thermal evolution of the system. Consequently, simulations that allow the gas to cool should also include a prescription for converting gas into stars; the *Cool+SF* simulation includes such a prescription for turning cold, dense gas into collisionless "star" particles. The technique and its computational implementation are described in detail by KWH. In brief, gas becomes "eligible" to form stars if it has a physical density corresponding to $n_{\rm H} > 0.1$ cm^{-3} and an overdensity $\rho/\bar{\rho} > 56.7$ (equivalent to that at the virial radius of an isothermal sphere). The gas must also reside in a convergent flow and be locally Jeans unstable, although the density criteria themselves are usually sufficient to ensure this. Eligible gas is converted to stars at a rate $d\ln\rho_g/dt = -c_\star/t_g$, where t_g is the maximum of the dynamical time and the cooling time. We use $c_\star = 0.1$ for the simulations here, but KWH show that the simulated galaxy population is insensitive to an order-of-magnitude change in $c_\star$, basically because the star formation rate is forced into approximate balance with the rate at which gas cools and condenses out of the hot halo. When star formation occurs, supernova heating is added to the surrounding gas assuming a standard IMF from 0.1 to 100M$_\odot$ and that stars above 8M$_\odot$ become supernovae. Each supernova adds 10^{51} ergs of thermal energy to the system. When a gas particle first experiences star formation, a fraction of its mass becomes stellar and the particle temporarily assumes a dual role as a "gas-star" particle, with its contribution to gas dynamical quantities dependent on its gas

mass alone. A gas particle is converted to a purely collisionless star particle when its gas mass falls below 5% of its initial value. As discussed in KWH, the use of hybrid gas-star particles allows us to avoid the computational cost of introducing extra particles into the simulation but also avoids decreasing the local gas resolution in cooling regions, which would happen if we immediately converted gas particles into star particles.

The initial gas particle distributions for the three SPH simulations are generated by taking the initial particle distribution for the *Dark* simulation and creating a gas particle for each high resolution dark particle. The gas particles are displaced from the dark particles by one-half of a grid spacing in each of the three directions. We assume a global baryonic fraction of $\Omega_b = 0.05$ consistent with nucleosynthesis values (Walker et al. 1991). The resulting grid has 44,000 gas particles, 44,000 high resolution dark matter particles, and 24,000 coarser resolution particles, for a total of 112,000 particles.

Finally, we evolve a very high resolution dark matter only simulation (*Hires*) by splitting each particle in the *Dark* simulation that fell within the virial radius of the cluster at $z = 0$ into 27 particles and extending the power spectrum down to smaller wavelengths. This simulation had a total of 1.3 million particles and was evolved using PKDGRAV (Stadel & Quinn 1998) with a gravitational softening length of $0.7h^{-1}$ comoving kpc (equivalent Plummer) and a dark matter particle mass of $\mathrm{M_{dp}} = 8.6 \times 10^8\,\mathrm{M_\odot}$.

All the results presented in this paper are at $z = 0$. The cluster virial radius, defined such that $\overline{\rho}(< \mathrm{R_{vir}}) = 178\rho_\mathrm{c}$, where ρ_c is average density of a critical universe, is $\sim 2\,\mathrm{Mpc}$ in all the simulations. The cluster virial mass is $4.1 \times 10^{14}\,\mathrm{M_\odot}$ and the circular velocity at the virial radius is $\sim 1000\,\mathrm{km\,s^{-1}}$.

4. Cluster Properties: 3-D Distributions

In this section we examined the physical properties of the simulated cluster averaged on spherical shells. During this section one must remember that the cluster is neither spherical nor even homogeneous on ellipsoidal shells. Interactively examining the structure of the cluster reveals sublumps, shocks and wakes whose properties are washed out in the spherical averages. For example, in the adiabatic simulation there is a sublump about 1 Mpc from the cluster center that has a higher pressure and density but whose temperature is slightly cooler than the surrounding medium (10^7K vs. a few 10^7K). Trailing behind this lump is a cooler "wake" (few 10^6K) extending out to the virial radius, which is in rough pressure equilibrium with the surrounding hot gas. Ahead of the lump is a shock front with particles as hot as 10^8K. Structures of this sort might conceivably be observable with the next generation of X-ray telescopes. Such substructure must also be kept in mind during the discussion when we refer to spherically averaged quantities.

4.1. Total and Dark Matter Distributions

In Figure 1, we plot the mean radial profile of the total (dark + baryonic) mass density in the cluster, relative to the universal density, ρ_c. The vertical bars along the x-axis denote the equivalent Plummer resolutions derived from the resolution lengths employed in the *Adiabatic*, *Dark*, *Cool+SF* and *Lowres* simulations. The heavier bars on top of the curves indicate the radii within which there are 32 particles; this can be considered the "mass resolution" limit of the simulation. At radii greater than $\sim 300\,$kpc, the cluster mass density profiles in the different simulations are indistinguishable. At the virial radius they fall as $\rho \propto r^{-3}$. The effects of resolution and the included physical processes are apparent at radii less than $\sim 300\,$kpc. The mass density profile in the *Lowres* simulation becomes increasingly shallower with decreasing radius, becoming nearly flat for $r < 60\,$kpc.

The radial mass profile for the higher resolution simulation (*Dark*), does not appear to differ significantly from the *Hires* simulation except perhaps at $r < 40\,\mathrm{kpc}$, suggesting that the total mass density profiles in these simulations are free from resolution effects for $r > 40\,\mathrm{kpc}$. This agrees with the conclusions of Moore et al. (1998). The total mass density profiles in simulations that include the same physical processes appear to converge at radii greater than our defined spatial resolution limit.

The inclusion of an adiabatic gas component does not significantly affect the total mass density profile on large scales. Differences do occur on small scales, however. The profile in the *Adiabatic* simulation slightly steepens within 60 kpc and then flattens substantially within 30 kpc, about the spatial resolution scale. The inclusion of cooling results in a significant change in the mass profile, with a rapid steepening within the central $\sim 100\,\mathrm{kpc}$, approximately 1.5 times the cooling radius in the *Adiabatic* simulation.

The mass density profile can be approximated by

$$\rho\,(r) = \frac{\rho_0}{(r/r_s)^{1.4}\,[1 + (r/r_s)]^{1.6}} \tag{1}$$

where $\rho_0 \sim 5900\rho_c$ and $r_s = 370\,\mathrm{kpc}$. This profile has the same inner slope of $\alpha = 1.4$ found by Moore et al. (1998), although the slope in the outer region is slightly steeper with $\alpha \sim 3$. [More recent high-resolution simulations of haloes of different masses all show an $\sim r^{-1.5}$ inner profile, turning over to r^{-3} at large radii (Moore et al. 1998, 1999).] Equation 1 matches the density profile of Navarro, Frenk & White (1997) at large radii but has a steeper central cusp.

We plot the difference between the profile in equation (1) and the density distributions of our simulations in Figure 2. The parameterization of equation (1) accurately describes the *Hires* simulation, and it reasonably describes both the *Dark* and *Adiabatic* simulations except in the very central regions where these flatten slightly. As indicated in Figure 1, both the *Lowres* and *Cool+SF* simulations have significant departures from the density

profile of equation (1).

The total mass density profile for the cluster in the *Cool+SF* simulation, even though it has the same spatial resolution as the clusters in the *Adiabatic* and *Dark* simulations, continues to rise steeply towards the cluster center and appears to steepen even further within the central 20 kpc. The density within the central 20 kpc exceeds that in the *Adiabatic* and *Dark* clusters by a factor of 14. This behavior is caused by additional physical processes, in the form of cooling, star formation and feedback, included in this simulation and is caused by baryons collecting in the cluster center. This pooling of baryons in the cluster center deepens the potential well and modifies the dynamics in that region.

In Figure 3, we show the radial density distribution for the dark matter component in each of the simulations. Since the *Dark* and *Hires* simulations are pure dark matter simulations, the curves appearing in this plot are identical to those in Figure 1. Interestingly, while all the simulations which include gas possess a very similar dark matter profile beyond ~ 30 kpc, within this radius it is apparent that *the additional physical processes of gas cooling and star formation result in a radical modification in the form of the dark matter profile*. This is not the case for those simulations where the gas was treated purely adiabatically, and the forms of the dark matter profiles for the *Adiabatic* and *Lowres* simulations are similar to those of their total mass distributions.

In each simulation with gas, the baryonic component represents a minor fraction of the mass at all radii. The only exception is the very central regions in the *Cool+SF* simulation, where the baryonic fraction approaches $M_b/M \approx 10$, revealing the bayonic nature of the central regions of this simulation. While enhanced with respect to the other simulations, the dark matter in *Cool+SF* comprises only half the total mass density at 20 kpc and even less further in.

4.2. Circular Velocity

The circular velocity of a test particle at radius r in a spherical mass distribution is given by

$$V_{circ}^2 = \frac{GM(<r)}{r}. \tag{2}$$

For an isothermal cluster, where the density falls as r^{-2}, the circular velocity is constant with radius. Figure 4 illustrates the radial dependence of the circular velocity for the simulations presented in this paper. As in the previous plots, the vertical bars indicate the two spatial resolutions. The circular velocities derived from the various simulations are compared to that derived from the profile of Navarro, Frenk and White (1997) defined such that

$$\begin{aligned} \rho(r) &\propto \frac{1}{r}\frac{1}{(a+r)^2} \\ V(r)^2_{NFW} &\propto \frac{1}{r}\left[\left(\frac{a}{a+r}\right) - 1 + \log\left(1+\frac{r}{a}\right)\right]. \end{aligned} \tag{3}$$

Such a profile is over-plotted in Figure 4, with $V_{max} \sim 1125\,km\,s^{-1}$ at a radius of $\sim 500\,kpc$. Unlike the total mass density profiles, which are identical at radii greater than $\sim 300\,kpc$, the circular velocities for the different simulations only converge at $r \gtrsim 1\,Mpc$ or slightly more than twice the nominal spatial resolution of the *Lowres* simulation. At the virial radius, the curves are very similar in form to V_{NFW}, decreasing as $r^{-\frac{1}{2}}$ with increasing radius.

For $r < 1\,Mpc$, the circular velocity curves begin to differ from one another. This is very apparent for the *Lowres* simulation; V_c is maximum at $\sim 1\,Mpc$ and drops to $\sim 85\%$ of its peak value of ∼1050km/s at the spatial resolution limit. The amplitudes of the other simulations all peak at ∼1100km/s at 600kpc. Apart from slight variations in amplitude, the remaining curves track each other until $\sim 200\,kpc$, where the circular velocity for the *Cool+SF* simulation stops declining as rapidly as the *Adiabatic*, *Dark* and *Hires* simulations.

The amplitudes and slopes of the latter three begin to diverge for $r \lesssim 200\,\mathrm{kpc}$.

Between $100\,\mathrm{kpc} \lesssim \mathrm{r} \lesssim 600\,\mathrm{kpc}$ the circular velocity of the *Cool+SF* simulation only decreases to $\sim 95\%$ of its peak value and then remains essentially constant until $\mathrm{r} \sim 20\,\mathrm{kpc}$, where it begins to rise towards the cluster center While this behavior is expected given the nature of the total mass density profile, this region is within the resolution limit of the simulation. Such high circular velocities in the central 20 kpc of clusters are probably incompatible with the observed dynamics of brightest cluster galaxies. Conceivably better resolution would resolve this discrepancy, but it may instead point to a shortcoming in our input physics. The difference between this curve and that of the *Adiabatic* simulation illustrates the impact of baryon dissipation on the structure of the cluster potential.

In sum, resolution affects the circular velocity out to typically 3 times the nominal resolution scale. The inclusion of an adiabatic gas component does not have much effect on circular velocities but a gas component that can cool and form stars causes the circular velocity to rise above pure dark matter calculations out to 200 kpc, about 3 times the cooling radius of the *Adiabatic* simulation.

4.3. Gas Density Profile and Baryon Fraction

In Figure 5, we plot the radial gas density profile for the cluster in the *Lowres*, *Adiabatic*, and *Cool+SF* simulations. The two adiabatic simulations approximately converge at $R \sim 300\,\mathrm{kpc}$, essentially the same as the convergence radius for the dark matter or total mass density profiles and corresponding to the nominal spatial resolution of the *Lowres* simulation. The gas density profile of the *Cool+SF* simulation, the one that includes cooling as well as star formation and its related feedback processes, does not converge to the gas density profiles of the adiabatic simulations until the virial radius ($\sim 2\,\mathrm{Mpc}$). We have

already commented how these processes affect the structure of the very central regions of the cluster, with dissipation producing a strong density peak in the center. This density peak has a strong influence on the cluster's X-ray properties, as we discuss in § 5.2 and §6 below. Figure 5 shows that cooling and star formation affect the gas density profile throughout the cluster, partly by deepening the potential well, partly by converting a significant fraction of the gas into stars, and partly because these two effects in turn alter the hydrodynamic evolution of the remaining diffuse gas.

Examining the profiles in more detail, one sees that all three gas density profiles have a slope of ~ 2.6 beyond the virial radius. At the virial radius the gas density profiles steepen, possibly indicating the presence of a weak shock. At 1 Mpc from the cluster center, both the *Adiabatic* and *Lowres* gas density profiles steepen to a slope of ~ 3.4. The steepening is less dramatic for the *Cool+SF* gas density profile which has a slope of ~ 2.7. Between 300 kpc and the virial radius $\rho_{Lowres} > \rho_{Adiabatic} > \rho_{Cool+SF}$; to first order caused by the response of the gas to the different potentials. In the *Lowres* simulation the central potential is shallower and the gas distribution is more extended. At 300 kpc, ρ_{Lowres} flattens to form a core and crosses the $\rho_{Adiabatic}$ profile, which continues to rise. At ~ 40 kpc, the gas density profiles of the *Cool+SF* and *Adiabatic* simulations also cross, owing to a combination of a rapid steepening of the *Cool+SF* density profile and a flattening of the *Adiabatic* profile. In the *Cool+SF* case, gas cools to form a galactic component, much of it found in the cluster center in the form of stars. This effectively depletes the hot intracluster medium and forms a giant galaxy in the cluster center. The redistribution of the gas has important consequences for the baryon fraction in the cluster. The causes and implications of these processes will be discussed in more detail in §6.

Figure 6 shows the fraction of the mass in baryons within a radius, R, normalized by $\Omega_{\rm b}/\Omega$, the mean baryon density of the universe, which was 0.05 in the simulations, i.e.

we plot $[M_b(< R)\Omega_{tot}]/[M_{tot}(< R)\Omega_b]$. We plot two curves for the *Cool+SF* simulation; the upper curve shows the distribution of the total baryonic component (in gaseous and stellar forms), and the lower curve shows the baryon fraction based only on the gaseous component.

The baryon fraction curves from the *Adiabatic* and *Cool+SF* simulations behave differently. As expected, both curves asymptote to unity as the radius approaches and exceeds the virial radius. However, going from the virial radius to the cluster center, the baryon fraction in the *Adiabatic* simulation declines gradually until $R \sim 24\,\mathrm{kpc}$ and then levels off at $\sim 20\%$ of the universal value. In the *Cool+SF* simulation, the baryon (total) fraction curve rises steeply towards the cluster center.

Looking at the gas fraction instead of the total baryon fraction in the *Cool+SF* simulation we find a very different result. Like the total baryon fraction in the *Adiabatic* simulation, the gas fraction in *Cool+SF* drops gently going from the virial radius towards the cluster center, leveling off at $\sim 240\,\mathrm{kpc}$. Moreover, the gas fraction in the cluster is significantly below unity at all radii and only climbs to 0.7 at twice the virial radius. The differences between the gas and the total baryon fraction curves in *Cool+SF* simulation indicates that 30% of the baryons in the cluster are locked up in stars and that the core of the cluster is, in fact, a stellar core. This is illustrated more graphically in Figure 7, where we plot the distribution of the individual baryonic components in the *Cool+SF* simulation; stars, hot gas ($\mathrm{T} > 10^{6.5}\mathrm{K}$) and cold gas ($\mathrm{T} < 10^{6.5}\mathrm{K}$). This plot is essentially unchanged when the boundary between hot and cold gas is reduced to $10^{4.5}\mathrm{K}$. Within 150kpc of the cluster center the baryons are dominated by stars, while beyond this radius, baryons exist mainly in the form of hot gas. Other than a small central peak and in galaxies , there is very little cold gas in the cluster; this has all been turned into stars.

4.4. Cooling Timescales

In Figure 8, we plot the cooling time as a function of distance from the cluster center. The cooling time is larger than the dynamical time at all radii in all three simulations. In the *Lowres* simulation none of the gas would cool within a Hubble time if cooling were suddenly included, something that might have led one to erroneously conclude that cooling is unimportant for the intracluster gas. Remember that in this and in the *Adiabatic* simulation cooling is not included during the evolution of the cluster. In the *Adiabatic* simulation, only within the central 70 kpc would the cooling time be shorter than the Hubble time (13 Gyrs) if cooling were suddenly included. Including cooling in this simulation would result in the eventual collapse of the gas within the central 70 kpc region.

In the *Cool+SF* simulation, the only simulation that included cooling during the evolution of the cluster, the cooling radius is actually smaller, only 40 kpc, because the gas density has been reduced by the conversion of gas into stars. With our star formation prescription, the injection of energy from supernova explosions has no significant effect on the thermal properties of the intracluster gas; the cooling time scale in the central regions is very short and cold gas is readily turned into stars. Any energy that is injected into the gas rapidly escapes radiatively. Beyond the central region ($\gtrsim 900\,\mathrm{kpc}$), sharp spikes are also apparent in Figure 8; these regions represents knots of cold, collapsed gas that correspond to galaxies within the cluster.

4.5. Gas Temperature

We plot the radial temperature profile of the gas averaged over a spherical shell in Figure 9. The temperature profiles for all the simulations are similar for radii greater than the virial radius, r $\gtrsim 2\,\mathrm{Mpc}$, more than 5 times the nominal spatial resolution scale of the

Lowres simulation. At smaller radii they exhibit quite different behavior, however. The *Lowres* simulation has the shallowest rise towards the cluster center, leveling off at a value of ∼2 keV in the central ∼ 800 kpc. The cluster in this simulation has a large isothermal core. The central temperature lies slightly below the virial temperature of $T_{vir} \sim 2.8$ keV.

The temperature profiles of the cluster in the *Adiabatic* and *Cool+SF* simulations begin to differ from one another within the central ∼ 1 Mpc. The temperature profile for the *Cool+SF* simulation rises steeply towards the cluster center where the gas temperature exceeds 6 keV. The temperature profile for the *Adiabatic* simulation rises less steeply, reaching a maximum temperature of only 4 keV in the cluster center.

The differences in the temperature profiles of the *Lowres* and *Adiabatic* simulations are caused by resolution effects, while the differences between the the *Adiabatic* and *Cool+SF* simulation result from the additional physical processes included in the *Cool+SF* simulation. Since one of these processes is cooling, we would have naively expected the gas in the *Cool+SF* simulation to be cooler towards the cluster center compared to the gas in the *Adiabatic* simulation. However, as we have already seen, the cooling time scale beyond 40 kpc is longer than a Hubble time; consequently, cooling cannot directly affect the gas beyond the very central region. The indirect effect of cooling is to lower the gas density outside of the core and to raise the central concentration of baryons, and the deepening of the cluster potential due to the latter has the overall impact of *raising* the gas temperature throughout most of the cluster. Within 40 kpc, the gas temperature does plummet from the peak value of ∼ 6.5 keV. We return to the impact of cooling on the cluster density and temperature profiles in §6.

Comparing the gas temperature profiles with the gas density profiles, the gas density, in all three simulations, is related to the gas temperature by $\rho_{gas} \propto T^3$ or equivalently, the pressure $P \propto \rho_{gas}^{4/3}$ for $r > 800$ kpc. In the central regions, the relationship approaches

$\rho_{\rm gas} \propto {\rm T}^{3/2}$ or ${\rm P} \propto \rho_{\rm gas}^{5/3}$, the relationship for an isentropic gas. Between 800 kpc and 40 kpc the pressure-density relationship can be approximated by ${\rm P} \propto \rho^{1.2}$. These scaling relationships break down in the very central regions of the *Cool+SF* cluster.

4.6. Gas and Dark Matter Entropy

In the top panel of Figure 10, we plot radial profiles of a quantity proportional to the entropy per unit mass for an ideal gas,

$$ {\rm S} = \log_{10}\left({\rm P}/\rho_{\rm gas}^{5/3}\right) \ , \tag{4} $$

where ${\rm P} = \rho_{\rm gas}{\rm k_B T_{gas}}/\mu{\rm m_H}$ is the gas pressure, $\rho_{\rm gas}$ is the gas density and $\mu{\rm m_H}$ is the mean molecular mass of fully ionized gas ($\mu = 0.6$). In all three simulations, the mean entropy per unit mass of the gas at $R > 3\,{\rm Mpc}$ (i.e. well beyond the virial radius) is quite high—comparable to the entropy per unit mass inside the cluster. Why does the gas have high entropy at such radii? One possibility, suggested by the results of Cen et al. (1995) and Cen & Ostriker (1999), is that the high entropy of the gas outside the cluster may due to the gas having been heated to temperatures of $10^5 - 10^7\ K$ by shocks associated with the formation of large-scale structures such as sheets and filaments. An alternative possibility is that the high entropy of the gas outside the cluster is due to numerical effects, as we discuss further below. We will address the origin of gas entropy in more detail in a subsequent paper. Here, it suffices to note that the entropy per unit mass inside and outside the cluster differ by a very small amount. Therefore, accretion shocks must produce only a small amount of entropy, suggesting that the cluster accretion shock is weak.

The gas entropy per unit mass in all three simulations differs within the virial radius. As we will discuss in §6, the total entropy of the gas in the three simulations is essentially the same. The profiles vary mostly because the gravitational potentials differ. That the

entropy profiles converge only at the virial radius highlights that differences in the potential, even if localized to the central 300 kpc of the cluster, can affect the gas distribution on scales of the entire cluster. The gas density profiles, as we already discussed, exhibit similar behavior. The entropy per unit mass decreases towards the cluster center, dropping from $S \sim 7$ at the virial radius to $S \sim 5.5$ at $r = 40\,\mathrm{kpc}$. In both the *Adiabatic* and the *Lowres* simulations, the intracluster gas forms a nearly isentropic core; in the *Lowres* simulation, the radial extent of the core is 300 kpc while radial extent of the core in the *Adiabatic* simulation is a factor of ~ 3 smaller.

In the bottom panel of Figure 10, we plot radial profiles of a quantity characterizing the "coarse-grain" entropy per unit mass for the dark matter,

$$\mathrm{S} = \log_{10}\left(\sigma_{\mathrm{1D}}^2/\rho_{\mathrm{dark}}^{2/3}\right) \ , \tag{5}$$

where ρ_{dark} is the local density of dark matter determined using the 64 nearest neighbours and σ_{1D} is the one-dimensional velocity dispersion of those particles.

On the whole, the dark matter entropy in all five simulations behaves similarly in the inner regions, declining from a value of ~ 5.5 at $\mathrm{r} = 0.8\,\mathrm{Mpc}$ to ~ 3.7 at $\mathrm{r} = 43\,\mathrm{kpc}$. Over this same radial range, the dark matter radial density profile scales as $\rho_{\mathrm{dark}} \propto \mathrm{r}^{-2}$ for $\mathrm{r} > 0.1\,\mathrm{Mpc}$ and $\rho_{\mathrm{dark}} \propto \mathrm{r}^{-1.7}$ for $\mathrm{r} < 0.1\,\mathrm{Mpc}$. If we define $\mathrm{P}_{\mathrm{dark}} \equiv \rho_{\mathrm{dark}}\sigma_{\mathrm{1D}}^2$, then $\mathrm{P}_{\mathrm{dark}} \propto \rho_{\mathrm{dark}}^{1.1}$ for $\mathrm{r} > 0.1\,\mathrm{Mpc}$, which is similar to the pressure-density relationship for the gas ($\mathrm{P}_{\mathrm{gas}} \propto \rho_{\mathrm{gas}}^{1.2}$). For $\mathrm{r} < 0.1\,\mathrm{Mpc}$, however, the pressure-density relationship for the dark matter shows a flattening trend ($\rho_{\mathrm{dark}}^{0.95}$ whereas that for the gas steepens to $\mathrm{P}_{\mathrm{gas}} \propto \rho_{\mathrm{gas}}^{5/3}$). The flattening of the dark matter pressure-density relationship is due to the combination of two effects: One, the density profile is flatter at $\mathrm{r} < 0.1\,\mathrm{Mpc}$ and two, the azimuthally-averaged dark matter velocity dispersion, which scales as $\mathrm{r}^{-0.1}$ for $\mathrm{r} > 0.1\,\mathrm{Mpc}$, turns over and decreases as $\mathrm{r}^{0.1}$ towards the cluster center.

Examining the dark matter entropy curves in detail, we note that the profile for the

Lowres simulation declines somewhat more gently towards the center than the corresponding profiles from the other simulations, a trend that appears to be directly correlated with the large force softening length in the *Lowres* simulation. The dark matter entropy profiles for the *Dark*, *Adiabatic* and *Cool+SF* also show a tendency to flatten on scales comparable to their respective force softening lengths. The entropy profile for the *Hires* simulation, which has much a smaller force softening length, shows no flattening.

At distances greater than $\sim 1\,\mathrm{Mpc}$ from the cluster center, the dark matter entropy profiles for four of the five simulations are similar. The only exception is the profile from the *Hires* simulation. Outside the cluster, the dark matter entropy in the *Hires* simulation is markedly lower than the entropy in the other simulations. We interpret the dark matter entropy outside the cluster as indicative of particle noise in the simulations. The particle noise is suppressed as the number of particles is increased, explaining the difference between results for the *Hires* and the other simulations. We note that since the number of dark matter particles and the number of gas particles in our simulations are equal, particle noise ought to contaminate both distributions to the same degree. In the case of the gas particles, however, artificial viscosity will convert the random motions due to noise into thermal energy when streams or shells cross, and it is possible that the high entropy of the gas beyond the cluster virial radius in the *Adiabatic* and *Cool+SF* simulations is due this type of particle noise heating.

Also, the dark matter profiles at distances greater than $\sim 1\,\mathrm{Mpc}$ have numerous troughs. These troughs are due to lower entropy dark matter in substructures. The *Hires* simulation exhibits the greatest degree of substucture and the corresponding entropy profile is highly serrated. In the three panels of Figure 11, we juxtapose the gas entropy profile and the dark matter entropy profiles. The offset between the two is mostly due to the difference in the dark matter and gas mass density. There is a high coincidence between the troughs

in the gas entropy and the dark matter entropy, again reinforcing the interpretation of the troughs in the dark matter distribution as being due to the presence of substructure. The number, the width and the depth of the troughs in the dark matter entropy profiles are directly related to the resolution of the simulations and the included physics. In comparing the *Adiabatic* and *Lowres* simulations, there are fewer troughs in the *Lowres* profile and the troughs are shallower and wider in keeping with the *Lowres* simulation having fewer, more "fluffy" clumps.

Comparing the behaviour of the dark matter and gas entropy in the three simulations with gas, we find that, except for an offset, the two track each other very well on scales $r > 0.2\,\mathrm{Mpc}$. The offset between the two is due to the fact that the dark matter density is larger than that of the gas and the dark matter temperature is typically lower than the gas temperature by a factor of 0.8. On smaller scales, however, the dark matter entropy profile continues to decrease towards the cluster center whereas the gas entropy curve, at least in the *Adiabatic* and the *Lowres* simulations, flattens to form a nearly isentropic core. (The gas entropy profile in the *Cool+SF* simulation also shows signs of flattening in the inner 0.1 Mpc but the steep decline in the gas entropy at the very center due to the cooling of the gas makes the comparison with the dark matter entropy less straightforward.) While this difference could be partly caused by caused by differences in numerical treatment of SPH and dark matter particles, we speculate that it is primarily a result of differences in the physical properties of the gas and dark matter components. In the case of the gas, short-range forces prevent colliding gas elements from interpenetrating, resulting in the formation of shocks. These shocks convert the kinetic energy of the gas into thermal energy; depending on the geometry of the shocks, the extent of acoustic waves generated by the shocks and the details of the artificial viscosity used in the simulations, the energy can be distributed over an extended region. Dark matter, on the other hand, is a collisionless fluid and will interpenetrate. This interpenetration can result in dark matter elements with

very different velocities occupying the same small but finite spatial volume, resulting in a "mixed" system. The coarse-grain entropy, as we have defined it, is a measure of how well the system is mixed in this sense. The dark matter entropy profiles of our simulated clusters indicate that the dark matter in the central regions is not as well mixed as in the outer regions. This is also borne out by the decline in the dark matter velocity dispersion on scales smaller than 0.2 Mpc. The extent of mixing depends on the initial state of the system as well as on constraints imposed by integrals of motion (Tremaine, Henon and Lynden-Bell 1986) and therefore, is likely to be affected by the physical characteristics of the system, such as the angular momentum distribution of the dark particles, as well as by numerical effects, such as particle and force resolutions.

5. Cluster Properties: Projected Distributions

Simulations of galaxy clusters have a wealth of structure on a range of scales. Observationally, however, we are restricted to a two-dimensional view of these systems, in the form of X-ray luminosity and temperature distributions, and maps of the projected surface mass density derived from the analysis of gravitational lensing features. In the following section we present the radial distribution of projected quantities. For this, we consider a box with a length of 4 Mpc on a side, twice the virial radius, centered on the deepest point in the cluster potential. All quantities are first smoothed in three dimensions with an adaptive SPH-like kernel over the 32 nearest neighbors. This smoothed distribution is then projected along the required axis [see Katz & White (1993)].

5.1. Total and Dark Matter Surface Mass Distributions

The left-hand column of Figure 12 plots the radial profiles of the the projected total mass density and the right-hand column plots the radial surface mass density profiles for only the dark matter. Each panel, labeled **X**, **Y** and **Z**, plots projections along one of the simulation axes; the total mass within the box is $1.3 \times 10^{15}\,\mathrm{M}_{\odot}$.

As expected from our analyses of the three-dimensional total and dark matter distributions in the different simulations, the projected total and dark matter mass distributions in the *Lowres* simulation appear similar. At large radii, the distributions fall off as $R^{-1.8}$, which agrees with what one would have expected given the three-dimensional distributions. Towards the cluster center, the profiles flatten, eventually forming a core, which again is not surprising given the nature of the three-dimensional profiles. However, the size of the core depends on the viewing angle. In the **X** and **Y** projections, the core begins to form at $\sim 300\,\mathrm{kpc}$, consistent with what one would have expected given the three-dimensional profiles, but in the **Z** projection the core is smaller by a factor of ~ 3 and the central surface density exceeds that in the **X** projection by a factor of ~ 1.6 and that in the **Y** projection by a factor of ~ 2.6. It appears that this enhancement is not due to the fortuitous presence of a subclump of matter along the **Z** axis but rather it is caused by the central regions of the cluster being ellipsoidal rather than spherical in shape with the major axis aligned along the **Z** axis.

The total and dark matter surface mass density profiles for the *Adiabatic* and *Dark* simulations are also very similar. There is a dependence of the core size and central peak projected mass density on the orientation of the cluster as seen in the *Lowres* simulation, although neither flatten enough to make a core in the central region. The projected mass density in the *Adiabatic* simulation has a slope of ~ 0.63 at radii less than 100 kpc in the **X** and **Y** projections while the projected mass density in the *Dark* simulation has a slightly

shallower slope of ~ 0.5. As in the *Lowres* simulation, the **Z** projection exhibits a markedly different behavior, with the *Adiabatic* simulation having a steeper slope of ~ 0.88 in the central regions and the *Dark* simulation having a slope of 0.66, both steeper than the slopes in the **X** and **Y** projections. The central projected mass density in the **Z** projection of the *Adiabatic* exceeds that of the other orientations by a factor of 1.7, while that of *Dark* simulation is 1.6 times higher.

The projected surface mass density profile in the *Hires* simulation is virtually indistinguishable from its lower resolution counterpart, the *Dark* simulation. The projected dark matter and total mass distributions in the *Cool+SF* simulation are similar to the corresponding projections of the *Adiabatic* and *Dark* simulations for $R \gtrsim 50\,\mathrm{kpc}$. At smaller radii, however, the total surface mass density exhibits a sharp up-turn, with a slope of ~ 1.15. This peak is not as prominent in the dark matter projections and is caused by the large central galaxy. Examining the profiles more closely, while both the total and dark matter surface density profiles in the **X** and **Y** projections are indistinguishable from the corresponding *Adiabatic* and *Dark* profiles beyond the central peak region, the projected mass density profile of the *Cool+SF* simulation in the **Z** projection lies below that of the *Adiabatic* and *Dark* profiles at clustercentric distances up to $\sim 200\,\mathrm{kpc}$. As in all the other simulations, the central surface density in the **Z** projection is greater than that in the other two projections, although the **Z** excess is only a factor of 1.25 in this case.

Even though the mass within the virial radius is the same in each simulation, each exhibits different lensing signatures. It is possible for the *Dark* cluster to be super-critical to gravitational lensing, producing giant arcs, while the *Lowres* simulation lies below the critical mass threshold and produces no strong lensing features. The gravitational lensing characteristics of a galaxy cluster, such as the radial positions and widths of giant arcs and the distribution of weakly lensed images, depend on the core radius and central value

and slope of the projected mass distribution (e.g. Hammer 1991), not on the total cluster mass. A small, but very centrally condensed, galaxy cluster can produce a much stronger lensing signal than a more massive cluster that is very diffuse. Using collisionless N-body simulations, Bartelmann et al. (1998) argue that the observed incidence of large arcs in clusters rules out most of the parameter space of CDM models, leaving only those models with low $\Omega_{\rm matter}$ *and* low Ω_Λ. They note that the effects of cD galaxies are a source of uncertainty in their conclusion, and our results suggest that the effects of radiative cooling and star formation could easily move some cosmological models from the "unacceptable" category to the "acceptable" category.

Due to differences in the projected mass distributions the simulated galaxy clusters have a lensing signature that depends on the viewing angle. Therefore, the mass distribution inferred from an analysis of the gravitational lensing characteristics would also depend on the viewing angle. The X-ray profile, which we discuss in detail in the next subsection, does not depend strongly on the viewing angle and has about the same profile when viewed from all angles. This might partially explain the observed discrepancy between cluster masses derived from gravitational lensing techniques versus those derived from X-ray analyses (e.g. Allen 1998) and will be addressed more carefully in a forthcoming paper.

5.2. X-Ray Surface Brightness

As illustrated in Figure 9, the gas that permeates the galaxy cluster has a temperature of several keV, and such an ionized medium emits copious amounts of X-rays. Over the last two decades, observations of galaxy clusters with space-borne X-ray telescopes have provided important insights on the physical properties of intracluster gas. With the assumption of spherical symmetry and isothermality, a "fundamental plane"-like relation between the X-ray luminosity, temperature and mass (e.g. Edge & Stewart 1991) has been

used to probe the cluster potential, making X-ray analysis one of the primary tools for investigating clusters.

The inclusion of a baryonic component into the simulated clusters allows us to similarly study such X-ray characteristics. The temperature and density of the gas is used, via a Raymond and Smith plasma code (Raymond & Smith 1977), to determine the X-ray emission at any location in the cluster. We project this emission along three orthogonal lines of sight, as we did with the mass distribution, to produce two-dimensional X-ray surface brightness maps using the SPH spline kernel smoothing [see Tsai et al. (1994) for details]. We assume the metal abundance of the gas is 0.3 Solar—a value considered typical for galaxy clusters (Mushotzky & Loewenstein 1997).

We plot the X-ray surface brightness distributions for the simulated clusters in Figure 13. The left-hand panels plot the surface brightness distributions for a $2 \rightarrow 10$ keV bandpass, similar to the ASCA Gas Imaging Spectrometers (GIS). We have not, however, filtered the X-ray surface brightness with any instrumental response functions and one should consider this to be a "raw X-ray" view of the cluster in this bandpass. This also allows a comparison to the X-ray luminosities in recently tabulated surveys of galaxy clusters [e.g. David et al. (1993)]. The right-hand panels plot the X-ray surface brightness distributions for a $0.1 \rightarrow 2.4$ keV bandpass similar to the ROSAT X-ray telescope filtered with the response function of the High Resolution Imager (HRI); these can be considered a true X-ray telescope view of the simulated cluster.

For *Cool+SF*, *Adiabatic* and *Lowres* simulations, the X-ray luminosity of the clusters in the $2 \rightarrow 10$keV bandpass are 3.14, 2.58 and $0.88{\times}10^{43}$ erg s^{-1} respectively (these are also summarized in Table 3). In the same band pass the Virgo cluster has an observed X-ray luminosity of $L_x = 1.16 \times 10^{43}$ erg s^{-1}, with a bolometric luminosity of $L_x^{Bol} = 2.66 \times 10^{43}$ erg s^{-1} (David et al. 1993). The X-ray flux in this same bandpass is

within a factor of three of this observed value for all the simulated clusters.

As with the total X-ray flux, the X-ray surface brightness profiles depend on the details of the simulation, but for each simulation these profiles have generic features that are independent of both the orientation and the energy band under consideration. Beyond 1 Mpc, about half the virial radius, all the X-ray surface brightness profiles are similar. Within the inner $\sim 300\,\mathrm{kpc}$, the *Lowres* simulation profile rapidly turns over, forming a flat X-ray core. The X-ray surface brightness in the *Adiabatic* simulation continues to rise all the way into the center of the cluster, slowly turning over but never fully flattening to form an apparent core. The X-ray surface brightness profile of the *Cool+SF* simulation falls below the others for $R \lesssim 1\,\mathrm{Mpc}$. Then, rising slowly, it crosses the X-ray surface brightness profile of the *Lowres* simulation inside its core. Within the central 50 kpc, about the cooling radius in the *Adiabatic* simulation, the profile of the *Cool+SF* simulation rapidly rises above the profile of the *Adiabatic* simulation. The cluster in the *Cool+SF* simulation has a bright X-ray core, a factor of 10 brighter than the central value in the *Adiabatic* simulation.

The *Cool+SF* X-ray surface brightness profiles have a number of additional X-ray "spikes" caused by emission from cooling gas associated with galaxies. Such systems cannot form in the *Adiabatic* and *Lowres* simulations. However, superimposed upon their smoother profiles, one can identify additional bumps. These are associated with a prominent peak in the *Cool+SF* distribution. These deviations are caused by the interaction of the intracluster medium with a merging subclump.

In contrast to the projected mass density profiles, the viewing angle has very little effect on the shape or normalization of the X-ray profiles. The only exception is the location of the galaxy peaks in the *Cool+SF* profiles. The slopes of the X-ray profiles do depend on the energy band, however.

To summarize, resolution affects X-ray surface brightness profiles within the nominal

spatial resolution scale, flattening them to form a core. The addition of cooling and star formation affects the X-ray surface brightness profiles out to one half the virial radius, both reducing their brightness and changing their shape to an approximate power law. Within the cooling radius, the profiles in the simulation with cooling and star formation rapidly rise, forming a bright X-ray core. Such sharp central peaks are observed in a substantial fraction of galaxy clusters and are interpreted as the observational consequence of a cluster "cooling flow" (see, e.g., Fabian 1994); whether or not this is the case in our simulated clusters will be addressed in §6.

The X-ray surface brightness distributions of observed galaxy clusters are often fit by a simple parameterized model given by

$$\mathrm{I_x} \propto \left[1 + \left(\frac{\mathrm{r}}{\mathrm{r_c}}\right)^2\right]^{\frac{1}{2}-3\beta}, \tag{6}$$

where $\mathrm{r_c}$ is the core radius and β controls the slope of the profile. Observed clusters have core radii of $100 - 600$ kpc and $\beta \sim 0.7$ (Jones & Forman 1984). We fit this model to the $2 \rightarrow 10$ keV X-ray profiles in Figure 13. This model fits the *Lowres* simulation X-ray profiles with a core radius of 560 kpc and $\beta = 1.4$.

Figure 14 shows fits of the β-model to the three projected X-ray surface brightness profiles of the *Cool+SF* simulation (left-hand panel) and the *Adiabatic* simulation (right-hand panel). The presence of the central X-ray cusp (or bright galaxy) and the galactic spikes in the *Cool+SF* simulation complicates the fitting procedure. Following the analyses of X-ray emissions from XD clusters by Jones & Forman (1984), we excise the central cusp region. We also excise the galactic spikes. We use only those locations marked with a circled point in the fits. We fit two different β-models to the simulations: one uses the full range of the X-ray profile and the second uses only a restricted range, from 50 kpc to 750 kpc, approximately the range used for observed clusters (Peres et al. 1998). We superimpose these fits over the profiles in Figure 14 with the dot-dashed line corresponding to the fit over

the full range and the solid line to the fit over the restricted range. The β-models provide a reasonable fit to the data, with the fit over the restricted range accurately reproducing the X-ray surface brightness within 0.5Mpc (neglecting the central cusp in the *Cool+SF*). The result of fitting to the restricted data range decreases the core radius and causes the slope to become shallower, i.e. β changes from ~ 1 to ~ 0.7. Observationally, the fitting of X-ray profiles find a $\beta \sim 0.7$, while measurements of β considering the gas temperature and cluster dynamics yield a value of ~ 1 [e.g. Jones & Forman (1999)], a situation often referred to as the β-discrepancy. While several solutions to this problem have been put forward (Edge & Stewart 1991; Bahcall & Lubin 1994; Carlberg et al. 1996), the results found with our numerical simulation suggest that the situation may be resolved if X-ray profiles could be determined to larger radii [e.g. Navarro, Frenk & White (1995)]. The addition of cooling and star formation does not greatly affect the β-model parameters when the central region is excluded. In fact, the model parameters are much more sensitive to the range over which the fit is performed than to the inclusion of cooling and star formation.

5.3. X-Ray Temperature

In addition to measuring the X-ray brightness, recent advances in X-ray detector technology have provided satellite telescopes, such as ASCA, with increased spatial and spectral resolution, allowing the determination of X-ray emission weighted temperature maps of clusters (Markevitch et al. 1998). Such observations provide a more direct probe of the physical properties of the intracluster gas, revealing that the majority of clusters deviate substantially from isothermality and have strong temperature gradients, with many being a factor of two hotter in the central regions than at the virial radius.

Since the X-ray emissivity as a function of position in the simulated cluster is known, it is straightforward to use the three-dimensional temperature information to determine

the projected X-ray temperature profiles, weighted with the X-ray emission in the chosen bandpass, for the simulated clusters. We plot these temperature profiles in Figure 15. The temperature profiles depend on the energy band because the emissivity in each band samples gas at different temperatures.

In the $2 \rightarrow 10$ keV band the *Lowres* simulation exhibits an almost flat, isothermal-like profile. The emission weighted temperature of ~ 2 keV is slightly lower than the virial temperature of $T_{vir} \sim 2.8$ keV. In the outer parts, $r > 1$ Mpc, the *Cool+SF* and *Adiabatic* temperature profiles gradually decline, falling by a factor of ~ 2 between 1 and 4Mpc, and hence deviate from an isothermal temperature profile. Within 1 Mpc, about half the virial radius, both temperature profiles begin to rise, peaking at $\sim 2T_{vir}$ for the *Cool+SF* simulation and $\sim 1.4T_{vir}$ for the *Adiabatic* simulation. The *Cool+SF* temperature profile falls to $\sim 1.8T_{vir}$ in the very central regions due to the presence of a small amount of cold gas. The profiles in the *Adiabatic* and *Cool+SF* simulations are similar to the profiles observed in galaxy clusters (Markevitch et al. 1998). The simulations have mean emission weighted temperatures of $\sim 1.2T_{vir}$ for the *Adiabatic* simulation and $\sim 1.6T_{vir}$ for *Cool+SF* simulation. However, in contrast to the spherically averaged 3-dimensional temperature profiles shown in Figure 9, projection causes the X-ray emission weighted temperature to have a less dramatic rise towards the center of the cluster. Also, the resolution of X-ray telescopes tends to be rather poor and much of the structure seen in Figure 15 would not be resolved, resulting in an apparently shallower gradient in the observed temperature distribution.

In the ROSAT pass-band, the *Lowres* simulation no longer has an isothermal temperature profile but slowly rises to $0.7T_{vir}$ in the cluster center. Similarly, the *Adiabatic* simulation rises to $1.4T_{vir}$, while the *Cool+SF* simulation rises to $2T_{vir}$. In the very center, the temperature profile in the *Cool+SF* simulation drops sharply to $1.4T_{vir}$, again due to the

presence of cold gas. This decline is more pronounced in the ROSAT band, since it is more sensitive to emission from colder gas (remember that the X-ray spectrum has been filtered with the instrument response of the ROSAT/HRI camera). At $r \gtrsim 1.4\,\mathrm{Mpc}$, both the *Cool+SF* and *Adiabatic* simulations follow the temperature profile of the *Lowres* simulation, but within 1 Mpc both depart significantly, rising to peak temperature of $\sim 1.4 T_{\rm vir}$.

Finite numerical resolution affects the projected X-ray emission weighted gas temperature profile even on scales that are more than ~ 4 times the nominal spatial resolution scale. In the *Lowres* simulation this extends all the way out to the virial radius. Improving the spatial resolution by a factor of ~ 6 increases the mean emission weighted temperature of the cluster by almost 60%. Adding cooling and star formation increases the mean temperature by another 30%, to more than 1.5 times the virial temperature, and increases the central temperature by almost 50% over that found in the *Adiabatic* simulation.

5.4. Sunyaev-Zel'dovich Decrement

The bulk and thermal motions of the hot gas that pervades the cluster environment can affect the spectrum of the Cosmic Microwave Background (CMB) via Compton scattering. This induces an anisotropy in the observed CMB distribution, measured as a decrement in the Rayleigh-Jeans temperature of CMB radiation in the direction of the cluster (Sunyaev & Zeldovich 1972). Such Sunyaev-Zel'dovich decrements have been observed in several clusters at radio wavelengths [e.g. Myers et al. (1997)] , and more recently at sub-mm wavelengths (Lamarre et al. 1998), and are proving to be a useful probe of the intracluster medium, as well as offering clues to the values of cosmological parameters (Furuzawa et al. 1998).

The inclusion of a baryonic component in the simulations allows us to investigate the Sunyaev-Zel'dovich decrement in the synthetic clusters. Figure 16 plots the combined local kinematics and thermal Sunyaev-Zel'dovich decrement, $\Delta T/T$, as a function of radius (note that we do not consider the kinematic effect due to the bulk cluster motion). This quantity is independent of frequency in the Rayleigh-Jeans region of the spectrum. Each projection axis is the same as those in Figure 12. Only in the very outermost parts of the cluster, beyond the virial radius, does the decrement depend on the viewing angle, although even there the differences, and the Sunyaev-Zel'dovich signal, are small. In the central regions, $R < 400\,\mathrm{kpc}$, the individual profiles diverge, with the *Lowres* simulation turning over. Both the *Cool+SF* and *Adiabatic* simulations have decrements that continue to rise. Although the *Cool+SF* simulation appears shallower at larger radii, in the very center it peaks, with a central value similar to that of the more gently rising *Adiabatic* simulation. These features do not depend strongly on the cluster orientation. In the central regions of the cluster, the thermal component dominates the kinematic Sunyaev-Zel'dovich effect by an order of magntude. This is consistent with the small flow velocities ($\sim 50\,\mathrm{km\,s^{-1}}$) seen in this region.

6. Discussion

It is apparent from the previous Sections that both numerical resolution and input physics can affect the evolution of a simulated cluster. Here, we consider the impact of these individually.

6.1. Resolution

Examining Figures 1 and 3 one can see that changing the force resolution affects the total mass and dark matter profiles only within about twice the spatial resolution scale.

The *Lowres* and *Adiabatic* simulations have identical profiles beyond that point. The mass profiles of the *Lowres* simulation show a significant flattening that begins on scales of twice the force resolution. The *Adiabatic* mass profiles continue to rise but also eventually flatten, again on a scale about twice the spatial resolution. The *Dark* simulation, consisting of only dark matter, has the same spatial resolution as the *Adiabatic* simulation. Compared to the *Hires* simulation, which is also a pure dark matter simulation, but with a spatial resolution ten times smaller than the *Dark* simulation, once again both the total mass and dark matter profiles of each simulation are the same until approximately twice the *Dark* simulation spatial resolution scale, where the *Dark* simulation mass profiles flatten slightly and depart from the *Hires* simulation mass profiles. Moore et al. (1998) also find a continual steepening of the mass profile as the spatial resolution is increased in their dark matter only simulations, but the mass profiles eventually converge as the spatial resolution scale became small enough (at fixed mass resolution). However, they also find that the mass profile becomes steeper as the mass resolution is increased, which accounts for some of the differences in the mass profiles of the *Dark* and *Hires* simulations.

The degree to which particles can bind together gravitationally is limited by the hardness of gravitational interactions, resulting in deeper potentials for smaller softenings. But mass resolution also plays a part: the smaller the particle mass, the denser the central core can become, steepening the potential. As mentioned in Section 5.1, the steepness of the central core can affect the gravitational lensing characteristics of a cluster of galaxies [e.g. Bartelmann (1996)] and one might draw erroneous conclusions about the expected lensing signature from a model cluster if the mass profile has not converged.

While resolution affects the form of the mass density profile on scales of twice the spatial resolution, the cluster potential, which depends on the integrated mass profile, is modified on much larger scales. Therefore properties that probe the potential, such as the

circular velocity and the temperature, are affected more globally. In Figure 4, the difference between the central mass profiles of the various simulations leads to different circular velocity curves on scales approaching half the virial radius. The distribution of gas within the cluster environment also depends on the form of the cluster potential. In Figure 9, the shallower cluster potential in the *Lowres* simulation results in less compressional heating than the higher resolution simulation whose potential is deeper, causing the temperature to be affected out to the virial radius. Finally, the total X-ray luminosity of the cluster also depends on the resolution. The higher resolution *Adiabatic* cluster has, as expected, a higher X-ray luminosity than the *Lowres* cluster.

6.2. The Addition of Baryons

Before discussing the detailed evolution of the baryonic material in these simulations, it is prudent to investigate whether or not the gas is artificially heated by numerical effects, specifically two-body interactions similar to those responsible for heating and subsequent core collapse in stellar systems. Such effects were recently investigated by Steinmetz & White (1997), whose analysis revealed that such heating effects can significantly modify the properties and hence evolution of the gaseous component. The magnitude of this effect depends mainly on the mass of the dark matter particles, although the relative gas particle to dark matter particle mass can mildly influence the cluster evolution. Steinmetz & White (1997) demonstrate that if the mass of the individual dark matter particles is below that of a critical mass, given by $M_{crit} \approx 5 \times 10^9 \sqrt{T_6} M_\odot$, where T_6 is the temperature in units of 10^6K, then spurious heating affects should be unimportant. In the high resolution regions of our simulations, where the temperature is several keV, $M_{crit} \sim 4 \times 10^{10} M_\odot$; the masses employed in the simulation are $M_{gp} = 1.2 \times 10^9\, M_\odot$ and $M_{dp} = 2.2 \times 10^{10}\, M_\odot$, respectively. We conclude, therefore, that our simulations should be free from spurious two-body gas-dark

matter heating effects.

In comparison to the *Dark* simulation, including a baryonic component in the form of an adiabatic gas (*Adiabatic*) does not greatly affect the overall properties of the cluster. Looking at Figures 1 and 3, the total mass and the dark matter profiles both have a very similar form outside of a radius a few times the spatial resolution. Within this distance, the mass profiles of the *Adiabatic* simulation rise slightly more steeply than the *Dark* simulation, before flattening. The *Dark* profile continues to rise into the center of the cluster. As with the effects of resolution, this redistribution of matter in the cluster, and hence modification of the cluster potential, influences the evolution of the cluster on scales several times the spatial resolution.

6.3. The Addition of Cooling and Star Formation

The inclusion of additional physical processes in the form of cooling and star formation can radically affect the evolution and subsequent properties of a cluster. For example, consider the profiles of the total mass and dark matter distributions (Figures 1 and 3). The *Adiabatic* simulation flattens as it approaches the center, but the *Cool+SF* simulation continues to rise rapidly and has a central peak. Figure 7 indicates that this baryonic core is mainly stellar.

How did the baryons pool into the center? Two possibilities present themselves, both of which may be occurring in the simulated cluster. First, the dense gas at the center of the cluster can dissipate its energy by radiative cooling, collapse to very high density, and form stars – in essence, a "cooling flow" creates a massive central galaxy. Second, dynamical friction and stripping of subclumps as they plunge into the cluster center can deposit *stellar* material into the cluster core (Babul & Katz 1993). Before the cluster itself assembles,

cooling allows gas to condense into the centers of "subunits," individual galaxies or galaxy groups. If the gas is cold and dense enough, it turns into stars. As a subunit merges into the cluster its less dense outer parts, comprised mostly of dark matter, are tidally stripped first and deposited further out in the cluster. Dynamical friction drags the dense core of the subunit closer to the cluster center, where eventually the tidal field is strong enough to disrupt it, depositing this baryon rich material deep in the cluster potential well. This process can cause segregation of baryons towards the center of the cluster even if the cooling times in the cluster are long.

To fully differentiate between these possibilities one needs to trace the dynamical evolution of the baryonic material during the formation and subsequent evolution of the cluster. This is beyond the scope of this paper which focuses upon the end-point of the cluster simulations, but will be the subject of a forthcoming article in which the cluster properties will be traced through the earlier simulation outputs. We can, however, address the question of whether or not the *Cool+SF* simulation has a cooling flow at the present time. We plot the gas mass accretion rate through spherical shells into the cluster, defined to be $\dot{M} = 4\pi\rho_{gas}(r)r^2V_r(r)$, normalized by the rate required for the cluster to accumulate its mass of gas within the virial radius (e.g. $\Omega_{\rm B}{\rm M}_{\rm vir}$) steadily over a Hubble time (i.e. $\dot{M} \approx 1 \times 10^3\,{\rm M}_\odot/{\rm yr}$) in Figure 17. Each of the simulations has similar rates of accretion, with both the *Cool+SF* and *Adiabatic* simulations having essentially identical profiles into 40 kpc. Since there is no cooling in the *Adiabatic* simulation, this implies that presently there is *no* significant cooling flow in the *Cool+SF* simulation on a scale $\gtrsim 40$ kpc. Considering Figure 13, it is within this radius that the X-ray profiles of the *Cool+SF* simulations possess an X-ray cusp; when coupled with the increase in the mass accretion in this region, the evidence points towards the *Cool+SF* simulation possessing a cooling flow within 40 kpc. This scale is smaller than typical scale of the cooling region [150 kpc of the cooling flow clusters Peres et al. (1998)]. This cooling flow, however, has no significant impact on the

inflow of mass on larger scales, suggesting that the latter is the result of recently accreted material being brought to a halt and redistributed with the cluster.

We also examine the radial infall velocity of the gas in the three simulations. In Figure 18 we plot the ratio of the spherically averaged radial infall velocity to the dynamical velocity, defined as r/t_{dyn} where $t_{dyn} \equiv (G\bar{\rho}_{tot})^{-1/2}$. The mean radial infall velocity is approximately $350\,km\,s^{-1}$ at distance of 4 Mpc from the cluster center and scales roughly as $|V_r| \propto r$ from 4 Mpc to ~ 0.5 Mpc *in all three simulations*. Therefore, the characteristic time scale for the radially infalling flow over this range in radii is nearly constant at $t_{flow} \sim 10$ Gyr. For $r > 3$ Mpc, the flow time is equal to the dynamical time, and the flow can be characterized as gravitational infall. Inward of 3 Mpc, pressure forces begin to affect the flow, and the flow velocity drops below the dynamical velocity. At $r \sim 0.5$ Mpc, the radial velocity of the flow is only $\sim 50\,km\,s^{-1}$, and inward of 0.5 Mpc $|V_r|$ continues to decrease. In Figure 19 we plot the spherically averaged radial velocity of the gas divided by the local adiabatic sound speed, i.e. the Mach number. The flow undergoes a relatively rapid transition from subsonic to mildly supersonic flow in the region 2.5 Mpc $< r <$ 3.5 Mpc, suggesting that a weak accretion shock is in this region. This places the shock at a slightly larger radius than that implied by the rise in the gas density profiles. The main differences between the results for the *Lowres* simulation and the other two simulations are caused by the smaller sound speed in the *Lowres* simulation. In the very central regions, the *Lowres* simulation appears to have a radial outflow. This feature is well below the spatial resolution of this simulation and is a numerical artifact.

At ~ 1 Mpc the radial velocity of the dark matter component in each of the simulations has a strong dip, indicating a more rapid infall of material at this radius caused by a significant clump of material currently merging with the cluster. Closely examining the gas radial infall plots, the gas in both the *Lowres* and *Adiabatic* simulations has similarly

enhanced infall velocities at this radius, implying that the infalling clump contains both dark matter and gas. This feature, however, is not present in the gas of the *Cool+SF* simulation, as most of the gas in the merging clump has collapsed and turned into stars. Such infalling clumps, coupled with the action of dynamical friction, could represent a primary mode of transport of baryons into the central regions of the cluster.

What causes the differences in the gas temperature profiles between the *Cool+SF* and *Adiabatic* simulations? We conjecture that two processes, either singly or jointly, could be responsible for these differences. First, supernova feedback could have heated the gas. The radial profile of the cumulative baryon fraction (Figure 6) shows that a non-negligible fraction of the baryons is in the form of stars. As a result of long local cooling time scales, the energy injected by the associated supernova explosions might not be radiated away and might heat the gas. The second possibility is an indirect impact of cooling. Cooling allows some of the gas to collapse and form stars, removing its contribution from the pressure support of the intracluster gas. Much of this collapsed, stellar component forms the dense, dynamically significant object in the center of the cluster. The gravity from this object draws in both the dark matter and the gas in the cluster; the drawing in of the former manifests itself as a steepening in the dark matter density profile. The gas would be similarly drawn in but unlike the dark matter would suffer compressional heating. Due to the long cooling time scale, the resultant thermal energy would not be radiated away. There is cooler gas in the central object, as well as in other objects that one would identify as galaxies, but the scale of these objects is much smaller than the scale of the cluster, and cold, dense gas turns into stars.

The radial profiles of the entropy, $S(r)$, for the *Adiabatic* and *Cool+SF* simulations (see Figure 10) suggests that the major differences in the gas density and temperature profiles for the two clusters (outside the very central core region) are caused by compressional

heating of the gas being drawn adiabatically into the deep central potential rather than by supernova heating. It is as if a given mass (gas) shell at some radius R_1 and entropy $S\Delta M_g$ in the *Adiabatic* simulation has simply been moved to a radius $R_2 < R_1$ in the *Cool+SF* simulation. To verify that this is indeed the case, we determined the mean entropy per unit mass $[\int S(r)\ dM_g(r)/M_g(r < r_{vir})]$ between the clustercentric radius R and the virial radius, as a function of the gas mass in the same volume. This quantity is unaffected by star formation. Under the above hypothesis, the results for the *Cool+SF* and *Adiabatic* simulations should be indistinguishable. As shown in Figure 20 this is indeed the case, and the results for the *Lowres* simulation are the same. Since the mean entropy per unit mass of the intracluster gas in all three simulations is essentially the same, supernova feedback, present only in *Cool+SF* simulation, cannot be significantly affecting the intracluster medium. The differences in the gas density, gas temperature, and specific entropy profiles are caused by the differences in the nature of the potential wells and by the gas responding adiabatically to establish hydrostatic equilibrium in these potentials. Hence one can understand the distribution of gas in the various simulations in terms of individual shells of gas behaving adiabatically. This does not imply, however, that the intracluster gas has a uniform entropy distribution (e.g. Figure 10). The entropy profile depends on the accretion history of the gas, including the strength of shocks.

The gas distributions within the simulations presented here can be described by a polytropic equation of state with $\gamma \approx 1.1$-1.2. Such a conclusion was also reached for a sample of nearby X-ray emitting clusters using ASCA observations (Markevitch et al. 1998). In their study of cluster mass estimates using gravitational lensing and X-ray methods, Miralda-Escudé & Babul (1995) found that the assumption that the intracluster gas is isothermal (as was thought at that time) results in a discrepancy between the two mass estimates, while the assumption that the gas was polytropic with $\gamma \approx 1.1$ resolves the discrepancy. The similarity between these observational results and our simulations is

encouraging. The polytropic nature of the gas appears to be a robust result, since it occurs in all three simulations even though they differ in their resolution and in the included physical processes. We will further investigate the origin of such a distribution in our next paper, where we study the physics of cluster formation by examining the history of the dark matter and gas properties through the course of the simulation.

Unlike simple gravitational physics and the hydrodynamics of an adiabatic gas, the behavior of a gas that cools and forms stars could depend on the prescription one uses to model these processes in a simulation. Although the prescription used in the *Cool+SF* simulation may not be a completely accurate description of star formation, the analysis presented here shows that cooling and star formation cannot be neglected. Consider, for example, the X-ray flux from a simulated cluster. The X-ray luminosity for the *Cool+SF* simulation is $L_x \sim 3 \times 10^{43}$erg s^{-1}, about three times that measured for the Virgo cluster of galaxies (which the simulation was chosen to represent). This contrasts with the simulations of a $7 \times 10^{14}\,M_\odot$ cluster by Suginohara & Ostriker (1998), who find an X-ray flux of 7.4×10^{45}erg s^{-1} with a temperature of only 3 keV. Clusters with this temperature are observed to have a much smaller flux, by more than a factor of 10 (David et al. 1993). While the Suginohara & Ostriker (1998) simulations and the *Cool+SF* simulation presented here both allow gas to cool, theirs did not include star formation. Star formation turns cooler, dense gas into stars and removes it as a significant source of X-rays, and it appears that this additional physics goes a long way to repairing the discrepancy between predicted and observed X-ray properties found by Suginohara & Ostriker (1998). Therefore we do not require additional heating via conduction or an excessively high supernova rate to reproduce observed X-ray luminosities. However, while the reasonable X-ray properties of our simulated clusters are encouraging, it is also clear that these properties depend in detail on the resolution and physics of the simulation. In the *Cool+SF* simulation, the reasonable X-ray luminosity has been achieved through the removal of some of the X-ray emitting

gas by conversion into stars. The fraction of baryons in stellar form, however, is 30% as opposed to the observed ∼10% and even then, *Cool+SF* cluster has the largest total X-ray luminosity.

In previous simulations of clusters that have included cooling, but not the subsequent formation of stars, the pooling of gas into the cluster core has resulted in the formation of a bright central X-ray peak approximately 200 kpc in extent (Katz & White 1993; Suginohara & Ostriker 1998). As demonstrated here, the addition of star formation and supernova feedback into the baryonic component reduces the brightness and the size of the X-ray cusp but does not eliminate its formation. In our simulation, the X-ray cusp is the result of stellar baryons forming a central object massive enough to influence the dark matter profile significantly. On the basis of the X-ray surface brightness profile, the *Cool+SF* cluster most closely resembles the XD clusters studied extensively by Jones and Forman (1984). X-ray cusps are seen in $\sim 70\%$ of observed clusters, with the enhanced central emission interpreted as being due to a cooling flow (Peres et al. 1998). While the *Cool+SF* simulation does exhibit a central X-ray cusp as well as evidence for a cooling flow in the central 40 kpc, the flow has no significant impact on the kinematics beyond 40 kpc.

Even with the inclusion of cooling and star formation, simulated clusters of galaxies may not truly resemble 'real' galaxy clusters. However, this does not imply that the complex processes associated with baryonic matter can be neglected in numerical studies of galaxy clusters. If simulations with cooling and star formation do not reproduce the observed properties of galaxy clusters, it may be because a much more sophisticated treatment of cooling is required, both in physical modeling or numerical treatment, or it may be that the simulations neglect other important processes like magnetic fields permeating the intracluster medium or feedback from AGN. A similar conclusion was also reached by Suginohara & Ostriker (1998).

7. Conclusions

- Moore et al. (1998) demonstrated that changing the resolution of a simulation results in a change in the slope of the density profile within the spatial resolution scale. We confirm this for the simulations presented here and similarly find that the central density profile is approximately $\rho \propto r^{-1.4}$. With the inclusion of cooling and star formation, however, the form of the mass profile is radically different, having a very steep central cusp. The combination of this deeper central potential well and the reduction in gas density in the cluster's outer parts (because of conversion to stars) affects many of the cluster's physical and observable properties. Also, we find that our lower resolution simulation does not properly capture the central density profile, illustrating that sufficient resolution is required to obtain convergent results.

- The scaling of the three-dimensional gas temperature with gas density is similar to that deduced by Markevitch et al. (1998) for a sample of nearby X-ray clusters. This result appears to be independent of the details of the simulation. The gradient in the observed temperature profile depends on projection effects (as well as on the resolution of the X-ray telescope).

- The X-ray surface brightness profile and total luminosity depend sensitively on both resolution and physics. In the simulation where gas cools and forms stars, a bright central X-ray cusp develops in the X-ray surface brightness profile. The total X-ray luminosity is reasonable for a Virgo-like cluster; however, the fraction of baryons in the form of stars is 30%, which is higher than typical fraction in observed clusters by a factor of ~ 3. Central X-ray cusps are observed in $\sim 70\%$ of galaxy clusters and are interpreted as being due to cooling flows (Peres et al. 1998). While a flow is apparent in the *Cool+SF* simulation, its scale ($\sim 40\,\mathrm{kpc}$) is smaller than those typically seen in observed galaxy clusters ($\sim 150\,\mathrm{kpc}$). Based on the X-ray surface brightness profile,

the *Cool+SF* cluster most closely resembles an XD cluster.

- The fitting of β-models, a common practice in cluster mass determinations from X-ray data, is sensitive to the radial range over which the fit is made. In our simulations, the best fitting model out to beyond the virial radius has $\beta \sim 1$, but a fit over the restricted radial range typically observed yields $\beta \sim 0.7$. This suggests that the observed discrepancy between β measured from cluster X-ray surface brightness distributions and that determined from X-ray temperatures and cluster dynamics may be resolved if the fit to the observed X-ray surface brightness profile could be extended to large radii.

- The gravitational lensing characteristics of a galaxy cluster, such as the radial positions and widths of giant arcs and the distribution of weakly lensed images, depend on the core radius, central value, and slope of the projected mass distribution (e.g. Hammer 1991), rather than on the total cluster mass. We find, due to the non-spherical nature of the clusters in our simulations, that these properties also depend on cluster orientation with respect to an observer. Hence, the mass distribution inferred from an analysis of the gravitational lensing characteristics would also depend on the viewing angle. The X-ray profile, however, does not depend strongly on the viewing angle. This might help to partially explain the observed discrepancy between cluster masses derived from gravitational lensing techniques and those derived from X-ray analyses (e.g Allen 1998). The increased central concentration in simulations with radiative cooling and star formation may rescue some cosmological models that otherwise fail to reproduce the observed incidence of cluster arcs (cf. Bartelmann et al. 1998).

- Due to computational limitations, simulations of cluster formation that have included a baryonic component have usually treated it as a simple adiabatic gas. Given that gas in clusters must have undergone cooling, collapse and processing into stars, is

this assumption of adiabaticity valid? Within our prescription both cooling and star formation proceed rapidly, resulting in very little cold gas pervading the cluster environment. The remaining hot gas continues to behave as an adiabatic fluid (Figure 20). However, ignoring these processes does not result in the same cluster evolution. Significant differences exist in all cluster properties for the *Adiabatic* and *Cool+SF* simulations. In the latter, as gas enters the forming cluster its density rises, so it cools efficiently and turns into stars. The reduction in pressure support in the central regions causes more gas to pool into the center and undergo cooling. This modification of pressure support, coupled with the increasing central density caused by the accumulation of stars, dramatically influences many of the cluster properties on scales out to the virial radius. It is important to note, therefore, that while the prescription used in the simulations presented here may not completely describe the cooling and subsequent star formation in galaxy clusters, the effects of these processes cannot be neglected if one wishes to draw physical inferences from numerical simulations.

8. Acknowledgments

We would like to thank J. M. Gelb and E. Bertschinger for their N-body simulations, and J. Raymond for discussions on the details of his plasma code. We would also like to thank George Lake and Eric Linder for useful discussions and the anonymous referee for useful comments and suggestions that improved the clarity of the paper. This work was supported in part by the NCSA and SDSC supercomputing centers, by NASA Astrophysics Theory Grants NAGW-2422, NAGW-2523, NAG5-3111, NAG5-3820, NAG5-4242, and NAG5-4064, by NASA LTSA grant NAG5-3525, by NASA HPCC/ESS grant NAG 5-2213, and by the NSF under grant ASC 93-18185, as well an NSERC Research grant. GFL

acknowledges support from a Pacific Institute of Mathematical Sciences Fellowship. AB acknowledges the hospitality of the University of Washington.

REFERENCES

Allen, S. W. 1998, MNRAS 296, 392

Babul, A. & Katz, N. 1993, ApJ 406, L51

Bahcall, J. N. & Lubin, L. M. 1994, ApJ 426, 51

Barnes, J.E. & Hut, P. 1986, Nature, 324, 446

Bartelmann, M. 1996, A&A 313, 697

Bartelmann, M. & Steinmetz, M. 1996, MNRAS 283, 431

Bartelmann, M., Huss, A., Colberg, J. M., Jenkins, A. & Pearce, F.R. 1998, A&A 330, 1

Bryan, G. L. & Norman, M. L. 1998, ApJ 495, 80

Carlberg, R. G., Yee, H. K. C., Ellingson, E., Abraham, R., Gravel, P., Morris, S. & Pritchet, C. J. 1996, ApJ, 462, 32

Cen, R. & Ostriker, J. P. 1994, ApJ 429, 4

Cen, R. & Ostriker, J. P. 1999, ApJ 514, 1

Cen, R., Kang, H., Ostriker, J. P. & Ryu, D. 1995, ApJ 451, 436

David, L. P., Slyz, S., Jones, C., Forman, W., Vrtilek, S. D. & Arnaud, K. A. 1993, ApJ 412, 479

Edge, A. C. & Stewart, G. C. 1991, MNRAS 252, 414

Eke, V. R., Navarro, J. F. & Frenk, C. S. 1998, ApJ 503, 569

Evrard, A. E. 1990, ApJ 363, 349

Fabian, A. C. 1994, ARA&A 32, 277

Furuzawa, A., Tawara, Y., Kunieda, H., Yamashita, K., Sonobe, T., Tanaka, Y. & Mushotzky, R. 1998, ApJ 504, 35

Gelb, J. M. 1992, Ph.D. Thesis, M.I.T.

Gelb, J.M. & Bertschinger, E. 1994, ApJ, 436, 467

Ghigna, S., Moore, B., Governato, F., Lake, G., Quinn, T. & Stadel, J. 1998, MNRAS, 399, 146

Gingold, R.A. & Monaghan, J.J. 1977, MNRAS, 181, 375

Hammer, F. 1991, ApJ 383, 66

Hernquist, L. 1987, ApJS, 64, 715

Hernquist, L. & Katz, N. 1989, ApJS 70, 419

Jones, C. & Forman, W. 1984, ApJ 276, 38

Jones, C. & Forman, W. 1999, ApJ, 511, 65

Katz, N. & White, S. D. M. 1993, ApJ 412, 455

Katz, N., Weinberg, D. H. & Hernquist, L. 1996, ApJS 105, 19

Lamarre, J. M. et al. 1998, ApJ 507, L5

Lucy, L. 1977, AJ, 82, 1013

Markevitch, M., Forman, W. R., Sarazin, C. L. & Vikhlinin, A. 1998, ApJ 503, 77

Miralda-Escudé, J. & Babul, A. 1995, ApJ 449, 18

Metzler, C. A. & Evrard, A. E. 1994, ApJ 437, 564

Moore, B., Governato, F., Quinn, T., Stadel, J. & Lake, G. 1998, ApJ 499, 5

Moore, B., Quinn, T., Governato, F., Stadel, J. & Lake, G. 1999, *astro-ph/9903164*

Mushotzky, R. F. & Loewenstein, M. 1997, ApJ 481, 63

Myers, S. T., Baker, J. E., Readhead, A. C. S., Leitch, E. M. & Herbig, T. 1997, ApJ 485, 1

Navarro, J. F., Frenk, C. S. & White, S. D. M. 1995, MNRAS 275, 720

Navarro, J. F., Frenk, C. S. & White, S. D. M. 1997, ApJ 490, 493

Pearce, F. R., Thomas, P.A. & Couchman, H. M. P. 1994, MNRAS 268, 953

Peebles, P. J. E. 1970, AJ 75 13

Peres, C. B., Fabian, A. C., Edge, A. C., Allen, S. W., Johnstone, R. M. & White, D. A. 1998, MNRAS 298, 416

Quinn, T., Katz, N., Stadel, J. & Lake, G. 1998, ApJ, submitted, astro-ph/9710043

Raymond, J. C. & Smith, B. W. 1997, ApJS 35, 419

Schindler, S. & Böhringer, H. 1993, A&A 269, 83

Schindler, S. & Müller, E. 1993, A&A 272, 137

Stadel, J. & Quinn, T. 1999, in preparation

Steinmetz, M. & White, S. D. M. 1997, MNRAS 288, 545

Suginohara, T. & Ostriker, J. P. 1998, ApJ 507, 16

Sunyaev, R. & Zeldovich, Y. B. 1972, Comments Astrophys. Space Phys., 4, 173

Tsai, J. C., Katz, N. & Bertschinger, E. 1994, ApJ 423, 553

Thomas, P. A. & Couchman, H. M. P. 1992, MNRAS 257, 11

Tremaine, S., Henon, M. & Lynden-Bell, D. 1986, MNRAS 219, 285

Walker, T.P., Steigman, G., Schramm, D.N., Olive, K.A. & Kang, H.S 1991, ApJ, 376, 51

Fig. 1.— The radial dependence of the density of all matter, both the dark and baryonic components, in each of the simulations presented in this paper. The bars along the x-axis indicate the spatial resolution for the medium and low resolution simulations. The equivalent bar for *Hires* lies off the left of the figure. The heavy bars that cross the individual curves indicate the radius within which each cluster has only 32 particles.

Fig. 2.— The difference between the distributions in Figure 1 and the model given by Equation 1.

Fig. 3.— As in Figure 1, but plotting the radial dependence of only the dark matter density in each of the simulations. Again, the bars along the x-axis indicate the softening lengths for the medium and low resolution simulations, while the heavy bars indicate the radius within which the cluster has only 32 particles.

Fig. 4.— The radial dependence for the circular velocity in each of the cluster simulations. The bars along the x-axis indicate the spatial resolution for the medium and low resolution simulations. The thick solid line in this figure shows the circular velocity of a halo with an NFW profile.

Fig. 5.— The radial dependence of the gas density in each of the simulations. The bars along the x-axis indicate the softening lengths for the medium and low resolution simulations and the heavy bars crossing the curves indicate the radius within which the simulation has only 32 particles.

Fig. 6.— The radial dependence of the cumulative baryon fraction in each of the simulations. The two solid lines represent the *Cool+SF* simulation: the total baryonic content of stars and gas (top line) and only gas (bottom line). The bars along the upper x-axis indicate the spatial resolutions of the low and medium resolution simulations. The central cusp in the *Lowres* simulation is well within the 32 particle resolution limit.

Fig. 7.— The distribution of the various baryonic components in the *Cool+SF* simulation. Here, the density is in units of the critical density and the black line represents the total baryonic mass. The central peak is comprised mainly of stars (dark grey line), although hot gas (lighter grey line) becomes the dominant baryonic component beyond $\sim 130\,\mathrm{kpc}$. Other than a peak at the very center of the cluster, there is very little cold ($T < 10^{6.5}\mathrm{K}$) gas, represented by the lightest grey line, in the cluster. This has been converted into stars.

Fig. 8.— The cooling time scale for the intracluster gas in the three simulations with baryonic component. Note the change of scale from logarithmic to linear at 1Mpc. The sharp spikes apparent in the *Cool+SF* simulation are knots of cold, collapsed gas. This gas is being processed into stars and represents galaxies.

Fig. 9.— As in Figure 1 but plotting the radial dependence of the gas temperature in each of the simulations. The bar in the upper left-hand corner indicates the softening length for the low resolution simulation. The horizontal line shows the virial temperature of the cluster ($T_{\mathrm{vir}} \sim 2.8$ keV).

Fig. 10.— As in Figure 1, presenting the radial dependence of the gas entropy (top) and dark matter (bottom) per unit mass in each of the simulations. The bars along the x-axis indicate the softening length for the low and high resolution simulations. Note the change in scale from logarithmic to linear at 1Mpc.

Fig. 11.— A comparison of the gas and dark matter entropy distributions for each of the simulations with gas. Each presents the gas (thin line) and dark matter (thick line) entropy for *Cool+SF*, *Adiabatic* and *Lowres* simulations.

Fig. 12.— Each panel plots the projected surface mass density versus radius. The left-hand panels plot the total mass in the simulations, while the right-hand panels plot only the dark matter. The **X**, **Y** and **Z**'s denote the projection axes, which are aligned with the coordinate axes of the simulation. The overdensity is with respect to integrating a uniform density of $\Omega = 1$ through a line-of-sight of 4Mpc, the size of the box from which these projections were made.

Fig. 13.— The projected X-ray emission: the left-hand panel shows the flux radiated into 4π steradians in the $2 \rightarrow 10$ keV band and the right-hand panel shows the flux in the ROSAT/HRI ($0.1 \rightarrow 2.4$ keV) band. This band is "windowed" with the normalized response function of the HRI instrument.

Fig. 14.— The 2→10 keV X-ray surface brightness profiles for the *Cool+SF* (left) and *Adiabatic* (right) simulations; each panel displays the **X**, **Y** and **Z** cluster projections. The thick solid line in each panel plots the best fit β-model (eq. 6) over a restricted range from 50 kpc to 750 kpc, similar to that employed with real X-ray data, while the dot-dashed lines plots the best fit β-model over the full range of the data. To avoid the effects of the X-ray peaks in the cluster center and at the positions of galaxies on the mean profile of the *Cool+SF* simulation, we use only the circled points in the fits. The best fit values for $(\beta, \mathrm{r_c})$ for the *Cool+SF* simulation are (0.97, 218kpc) and (0.63, 72kpc) for the full and restricted range respectively. The corresponding values for the *Adiabatic* simulation are (1.07, 211kpc) and (0.77, 106kpc).

Fig. 15.— Like Figure 13 but plotting the projected X-ray emission weighted temperature profiles.

Fig. 16.— The projected Sunyaev-Zel'dovich decrement for the various cluster simulations.

Fig. 17.— The mass accretion rate of gas through spherical shells into the cluster normalized by the accretion rate required to accumulate the mass of gas within the cluster virial mass at the present time ($2.05 \times 10^{13}\,\mathrm{M_\odot}$) in a Hubble time. Note the change of scale from logarithmic to linear at 1Mpc.

Fig. 18.— The spherically averaged radial infall velocity of the gas divided by the local dynamical velocity, which we define as $\mathrm{r/t_{dyn}}$. Note the change of scale from logarithmic to linear at 1Mpc.

Fig. 19.— The spherically averaged radial infall velocity of the gas in units of the local sound speed. Beyond the virial radius a weak shock is present. Note the change of scale from logarithmic to linear at 1Mpc.

Fig. 20.— The total entropy in the cluster as a function of gas mass between a radius r and the virial radius. Both axes have been normalized by the mass of gas within the virial radius.

Table 1. A summary of previous numerical studies of galaxy clusters.

Ref.	Spatial (h^{-1}kpc)	Dark($h^{-1}\,M_\odot$)	Virial ($h^{-1}\,M_\odot$)	Gas($h^{-1}\,M_\odot$)	Cool / Star	$M_{clust}(h^{-1}\,M_\odot)$
(a)	150	3.0×10^{13}	5.6×10^{12}	3.4×10^{12}	N	$1.2\times10^{15}(<R_A)$
(b)	14	4.8×10^{11}	4.5×10^{9}	4.8×10^{10}	Y/N	$1.0\times10^{14}(<R_{200})$
(c)	$270h$ p	$1.1\times10^{14}h$	$3.3\times10^{13}h^3$	$2.2\times10^{11}h$	N	$1.85\times10^{15}h(<R_{200})$
(d)	40	3.8×10^{12}	1.1×10^{11}	4.2×10^{11}	Y/N	$5.9\times10^{14}(<R_{200})$
(e)	628	1.2×10^{11}	4.1×10^{14}	1.2×10^{10}	N	many
				(2.1×10^{12})		
(f)	78	2.0×10^{12}	7.9×10^{11}	2.2×10^{11}	N	$4.7\times10^{14}(<R_{400})$
(g)	50 p	9.4×10^{11}	2.1×10^{11}	9.4×10^{10}	N	$2.5\times10^{14}(<R_{200})$
(h)	50	4.8×10^{12}	2.1×10^{11}	2.6×10^{11}	N	3-20 $\times10^{14}(<R_{500})$
(i)	98	1.6×10^{10}	1.6×10^{12}	1.7×10^{9}	N	many
				(3.0×10^{11})		
(j)	14 p	2.3×10^{12}	4.5×10^{9}	2.6×10^{11}	N	$1.0\times10^{15}(<R_{200})$
(k)	66	8.0×10^{11}	4.8×10^{11}	4.9×10^{11}	Y/N	$>1.2\times10^{14}(<R_A)$

Note. — All values are for clusters at z=0. Physical, rather than comoving, resolution scales are denoted by a p; corresponding virial mass scales as $(1+z)^3$. The studies are: (a) Evrard (1990); (b) Katz & White (1993); (c) Schindler & Böhringer (1993); Schindler & Müller (1993); (d) Thomas & Couchman (1992); (e) Cen & Ostriker (1994); (f) Metzler & Evrard (1994); (g) Navarro et al. (1997); (h) Bartelmann & Steinmetz (1996); (i) Bryan & Norman (1998); (j) Eke et al. (1998); (k) Suginohara & Ostriker (1998).

Table 2. A summary of the various resolutions of the simulations presented in this paper.

Name	Spatial (h^{-1}kpc)	Dark Matter ($h^{-1}\,M_\odot$)	Virial ($h^{-1}\,M_\odot$)	Gas ($h^{-1}\,M_\odot$)	Cool/Star	$n_{dark}/n_{gas}/n_{star}$	$n_{timesteps}$
Dark	14	3.7×10^{11}	4.6×10^{9}	NO	NO	18134/0/0	2400
Cool+SF	14	3.5×10^{11}	4.6×10^{9}	1.9×10^{10}	YES	18221/11582/6987	2400
Adiabatic	14	3.5×10^{11}	4.6×10^{9}	1.9×10^{10}	NO	18290/17017/0	2400
Lowres	200	3.5×10^{11}	1.3×10^{13}	1.9×10^{10}	NO	17884/17708/0	2400
Hires	1.4	1.4×10^{10}	4.6×10^{6}	NO	NO	494486/0/0	10000

Cluster Vital Statistics: $M_{clus} = 2.1 \times 10^{14} h^{-1}\,M_\odot$, $R_{vir} = 1 h^{-1}$Mpc & $V_{circ}(R_{vir}) = 1000\,km\,s^{-1}$

Note. — Quantities are defined as in Table 1. Although we quote h^{-1} units to be consistent with Table 1, remember that $h = 0.5$ and that the "spatial resolution" is *twice* the gravitational softening length. The final column refers to the number of particles, and their type, within the virial radius.

Table 3. Cluster X-ray properties

Name	$L_x(10^{43}$erg s$^{-1})$	$\langle T_x \rangle$ (keV)
Cool+SF	3.14	4.41
Adiabatic	2.58	3.43
Lowres	0.88	2.16

Note. — A summary of the X-ray properties, in the 2→10 keV energy band, for the simulated clusters presented in this paper. The temperature is the mean emission weighted temperature averaged over a circle of radius of the virial radius (change this to twice or half the virial radius does not significantly alter either the X-ray flux or emission weighted temperature for the simulated cluster). The cluster virial temperature is 2.8 keV.

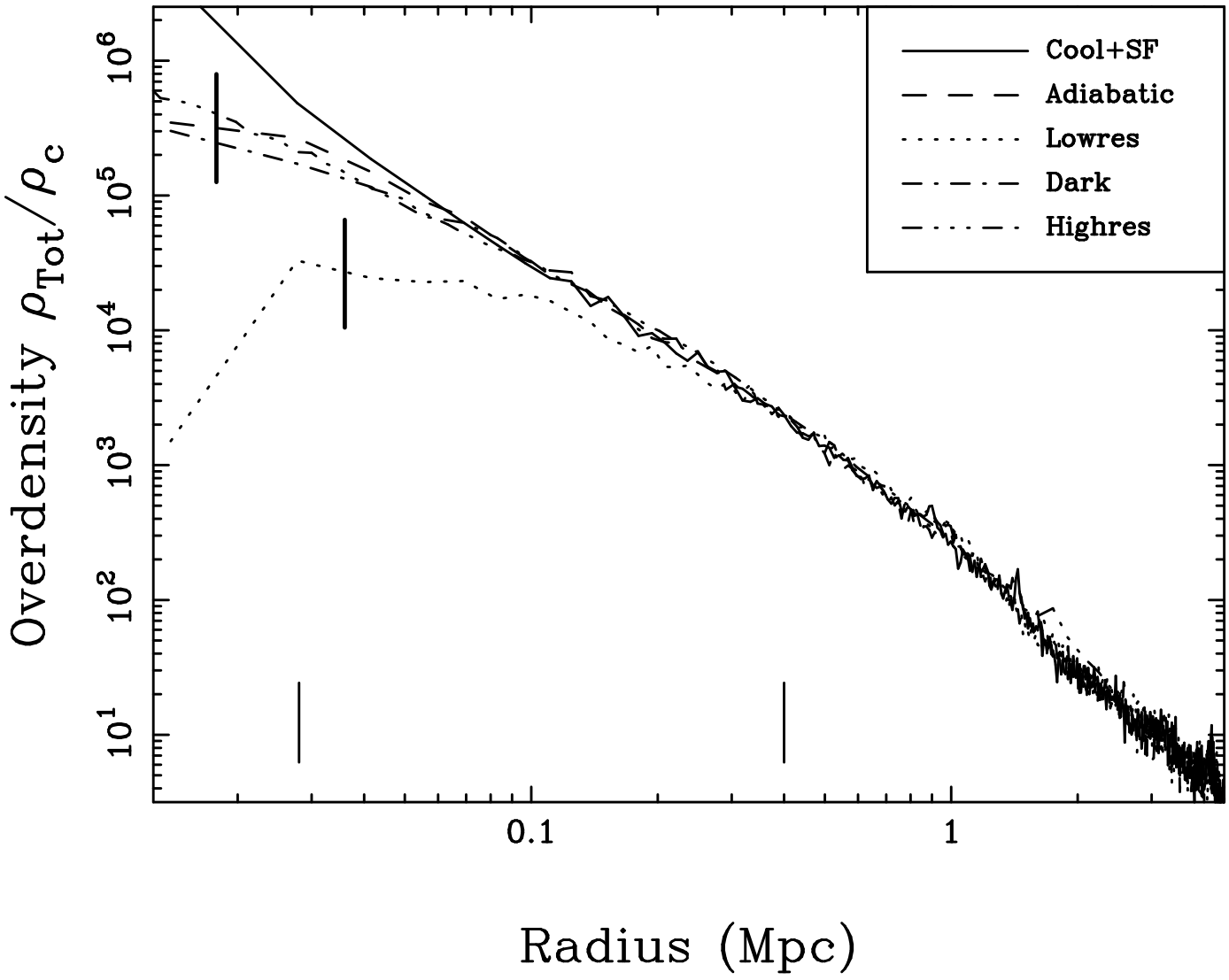
Cool+SF
Adiabatic
Lowres
Dark
Highres
Overdensity $\rho_{\rm Tot}/\rho_{\rm c}$
10^1
10^2
10^3
10^4
10^5
10^6
0.1
1
Radius (Mpc)

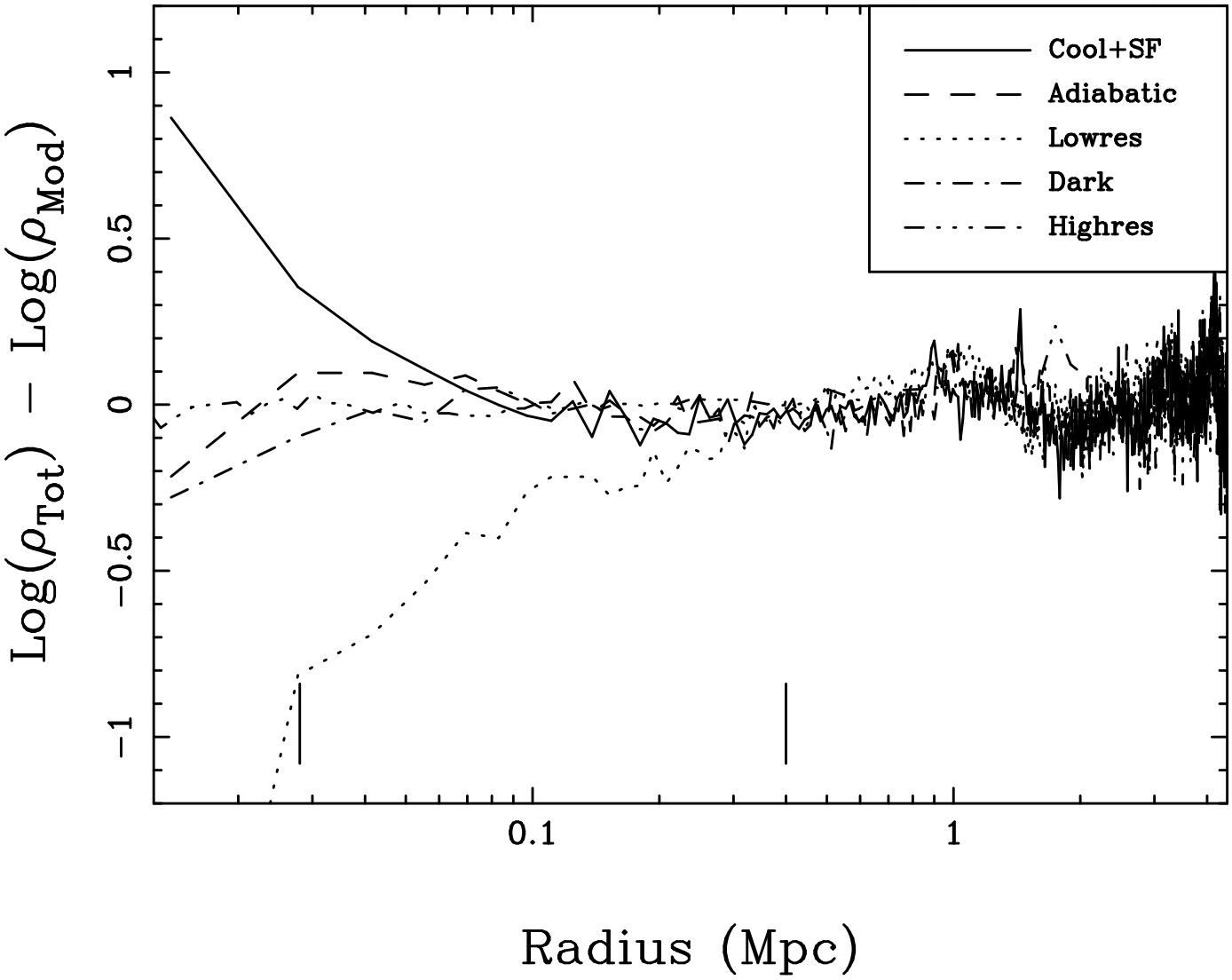
Cool+SF
Adiabatic
Lowres
Dark
Highres
Log(ρ_{Tot}) − Log(ρ_{Mod})
1
0.5
0
−0.5
−1
0.1
1
Radius (Mpc)

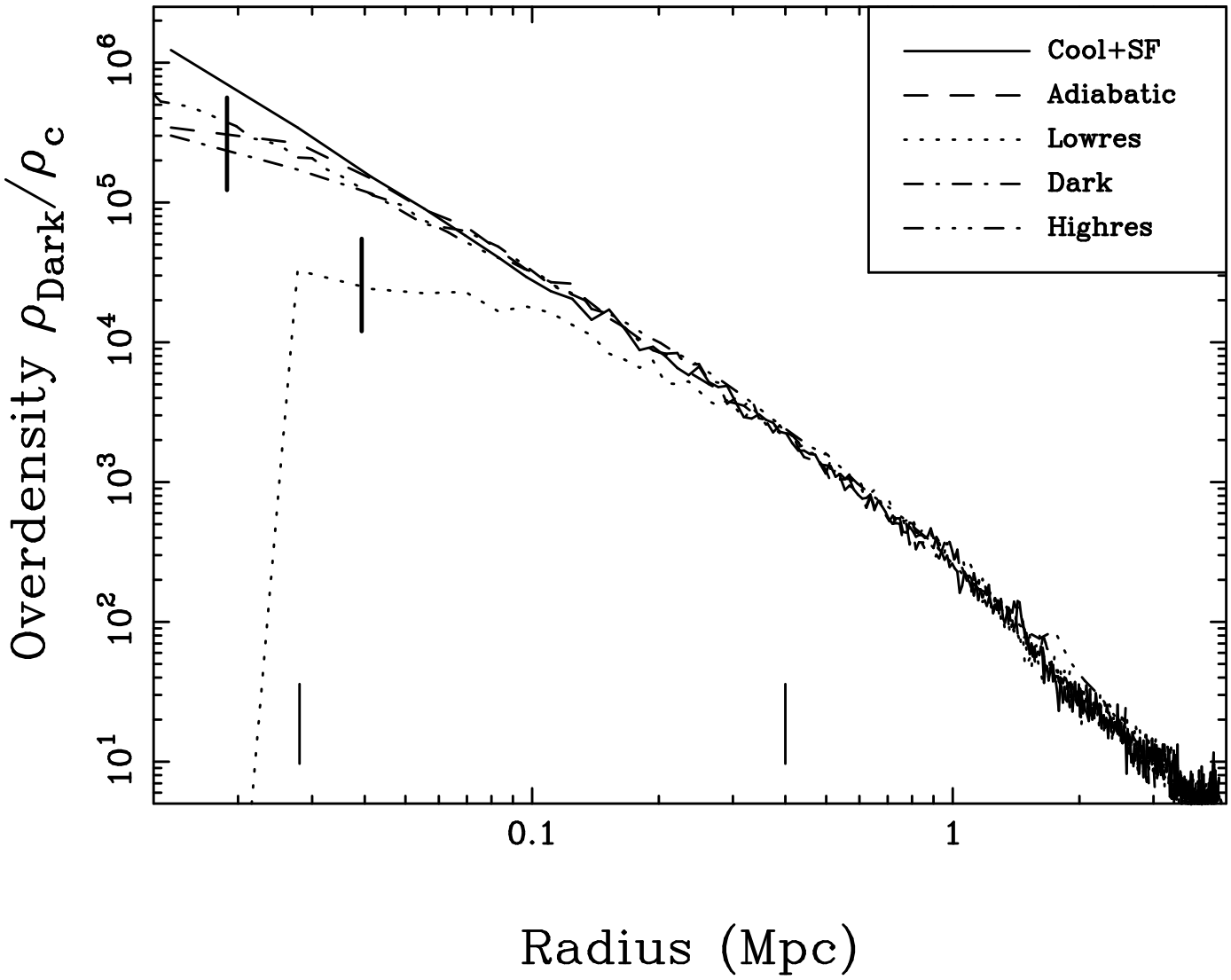
Cool+SF
Adiabatic
Lowres
Dark
Highres
Overdensity $\rho_{\rm Dark}/\rho_{\rm c}$
10^1
10^2
10^3
10^4
10^5
10^6
0.1
1
Radius (Mpc)

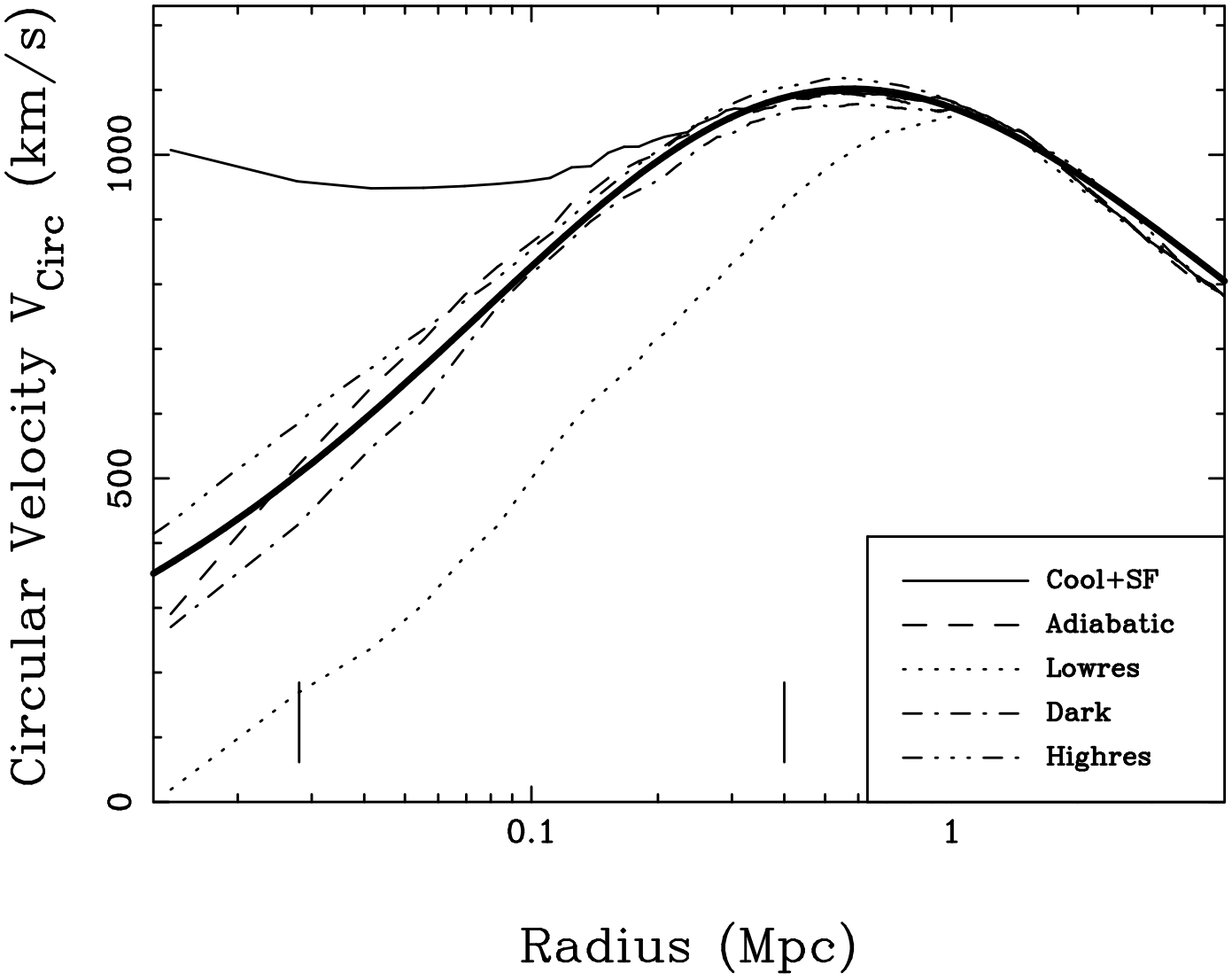
Circular Velocity V_{Circ} (km/s)
0
500
1000
0.1
1
Radius (Mpc)
Cool+SF
Adiabatic
Lowres
Dark
Highres

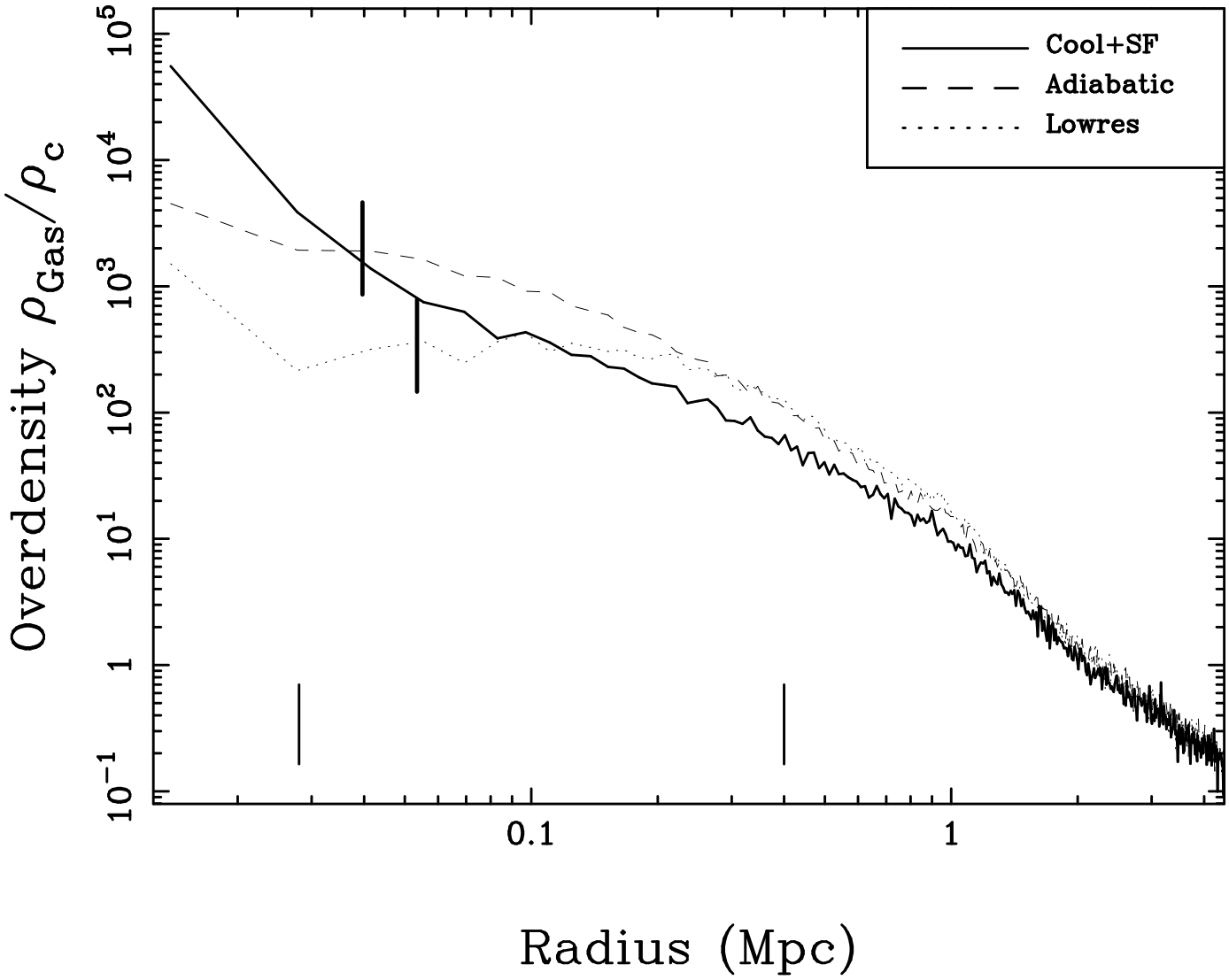
Cool+SF
Adiabatic
Lowres
Overdensity ρ_{Gas}/ρ_c
10^{-1}
1
10^1
10^2
10^3
10^4
10^5
0.1
1
Radius (Mpc)

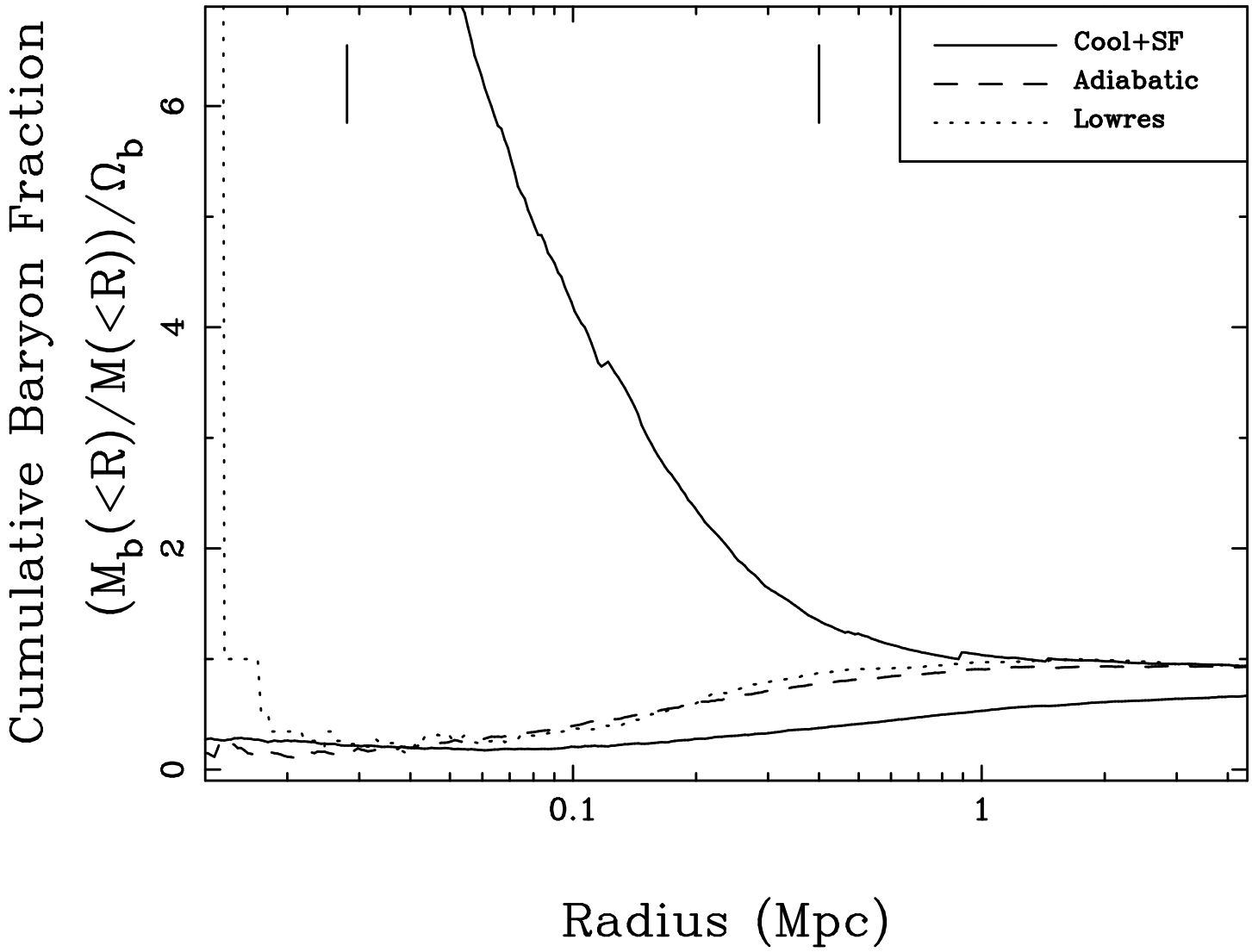
Cumulative Baryon Fraction
$(M_b(<R)/M(<R))/\Omega_b$
0
2
4
6
0.1
1
Radius (Mpc)
Cool+SF
Adiabatic
Lowres

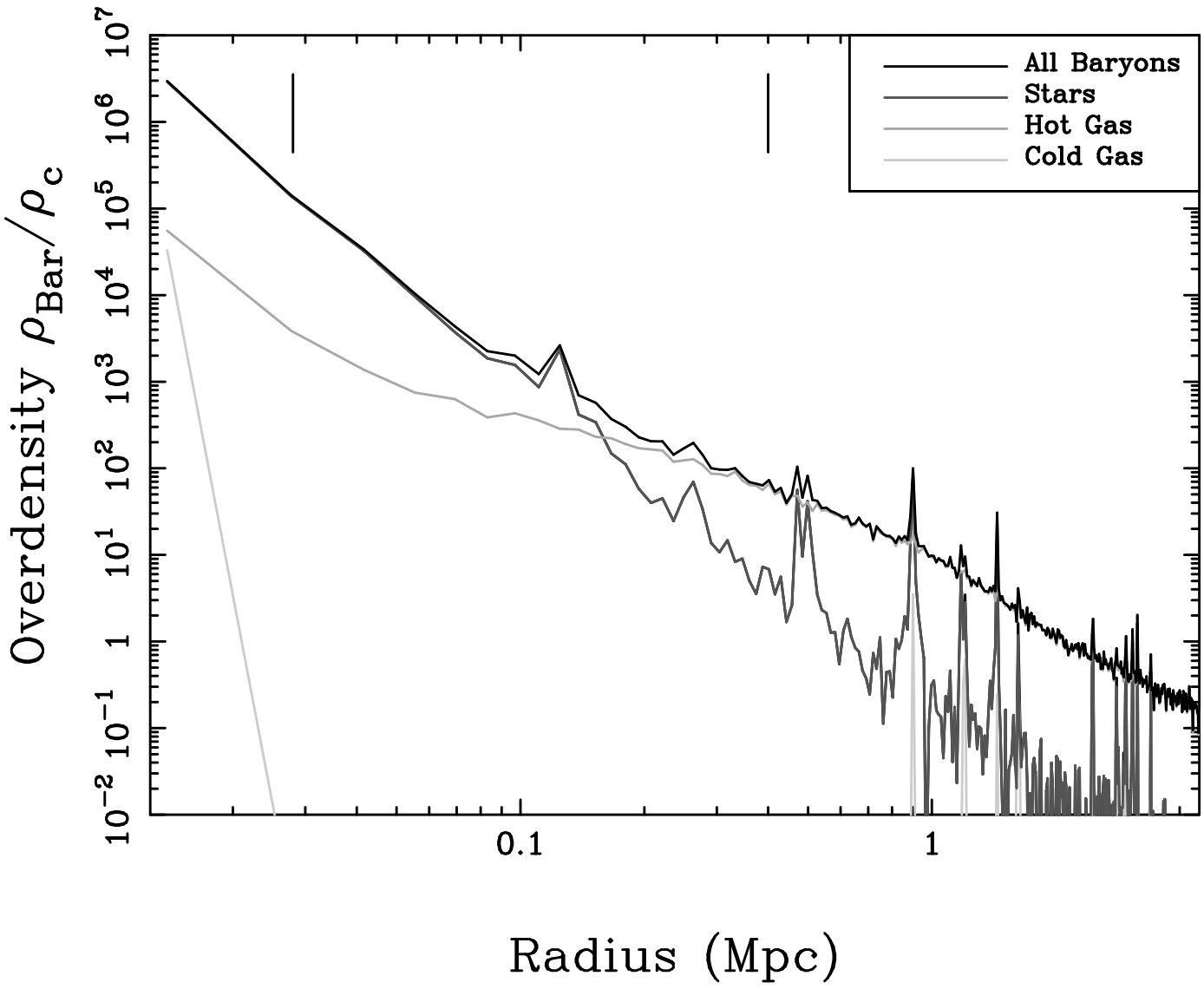
All Baryons
Stars
Hot Gas
Cold Gas
Overdensity ρ_{Bar}/ρ_c
10^{-2} 10^{-1} 1 10^{1} 10^{2} 10^{3} 10^{4} 10^{5} 10^{6} 10^{7}
0.1
1
Radius (Mpc)

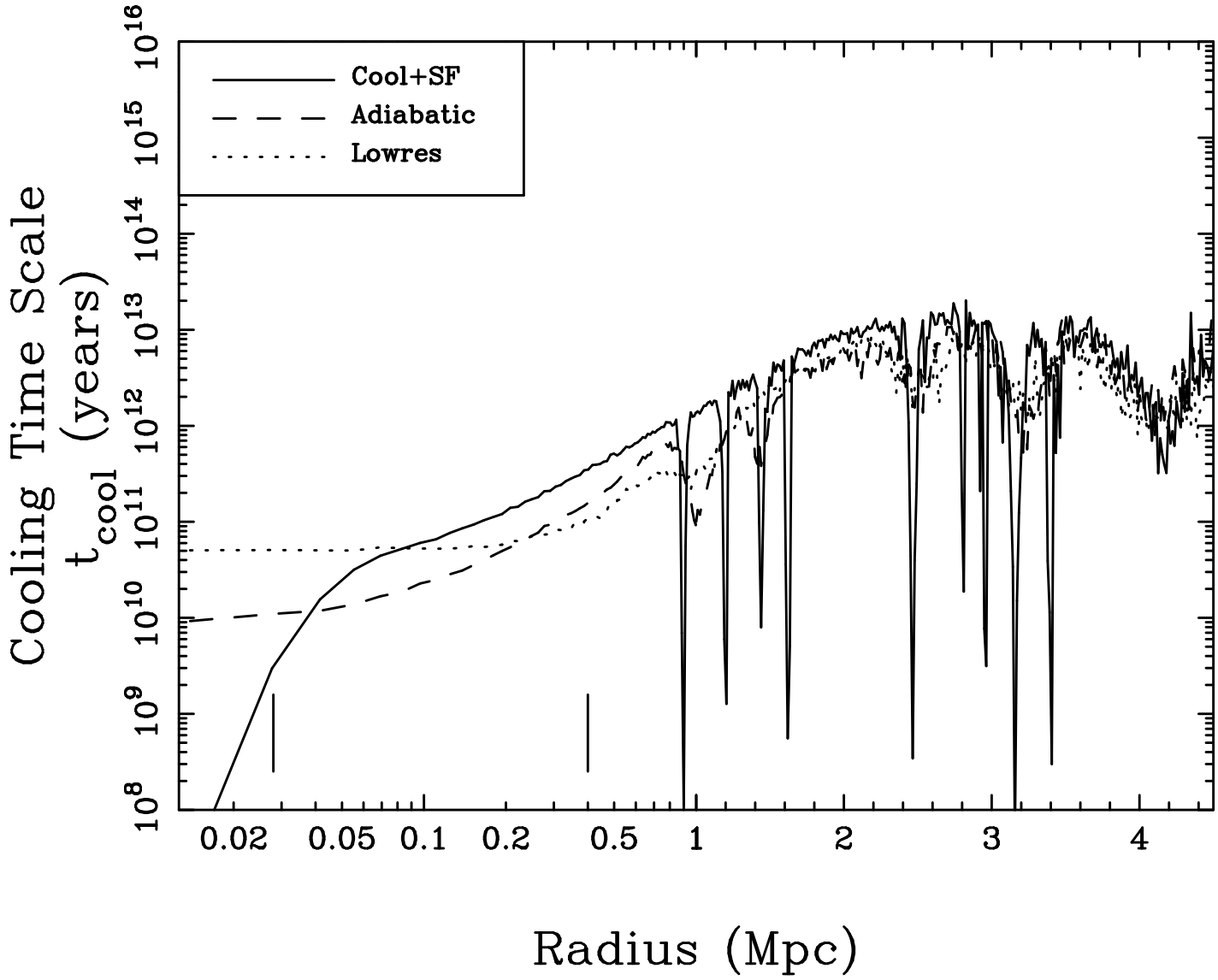
Cool+SF
Adiabatic
Lowres
Cooling Time Scale
t_{cool} (years)
10^{8}
10^{9}
10^{10}
10^{11}
10^{12}
10^{13}
10^{14}
10^{15}
10^{16}
0.02
0.05
0.1
0.2
0.5
1
2
3
4
Radius (Mpc)

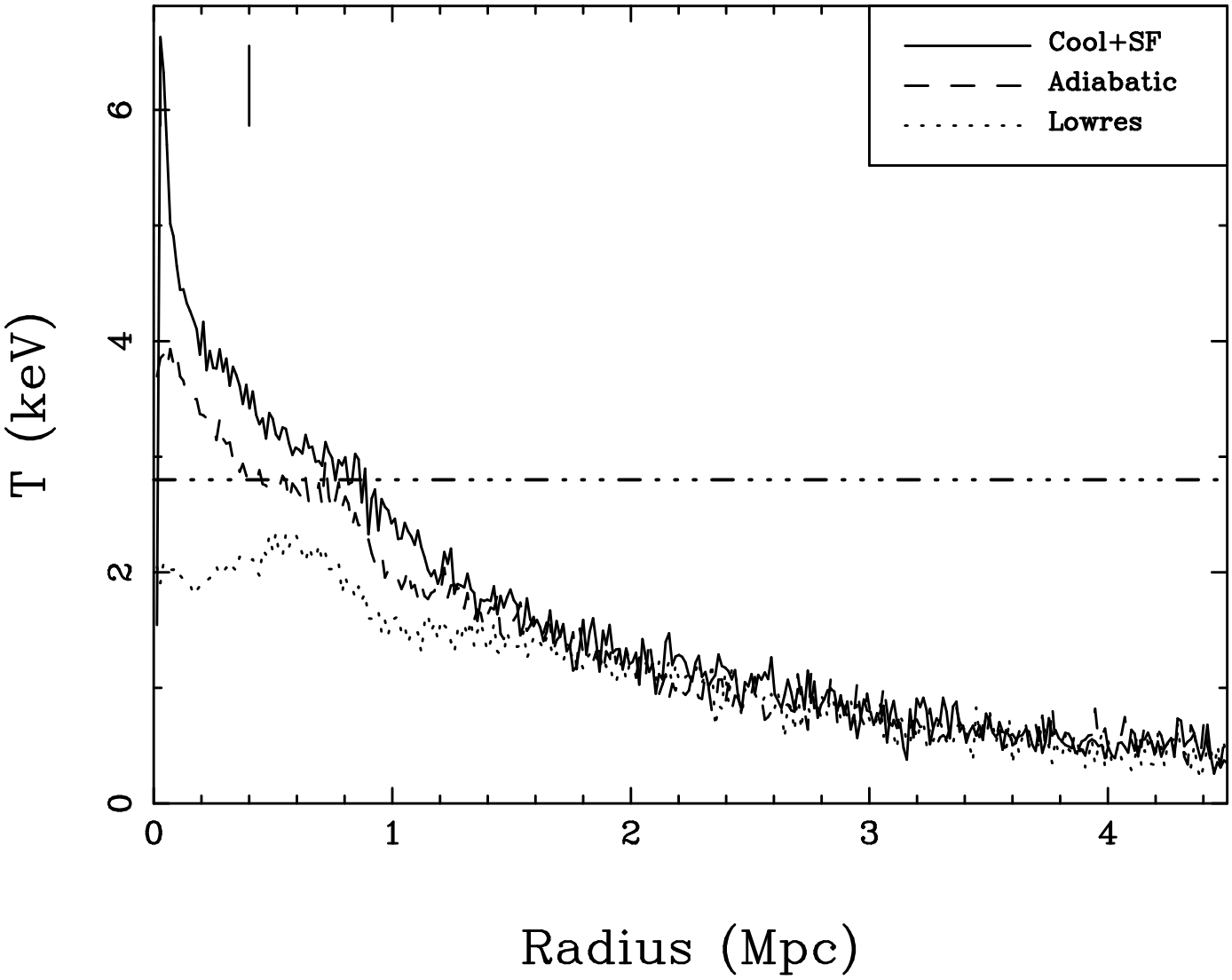
Cool+SF
Adiabatic
Lowres
T (keV)
0
2
4
6
0
1
2
3
4
Radius (Mpc)

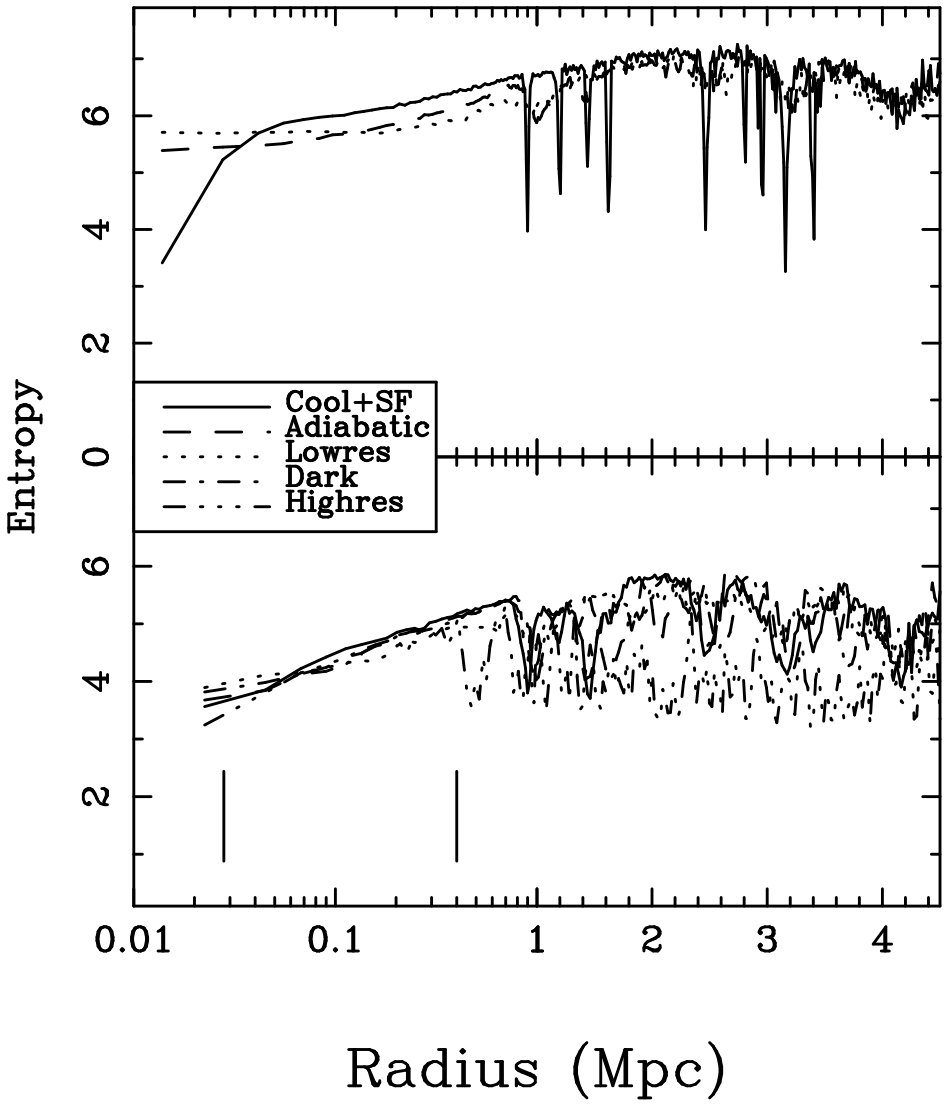
Entropy
Cool+SF
Adiabatic
Lowres
Dark
Highres
0
2
4
6
0.01
0.1
1
2
3
4
Radius (Mpc)

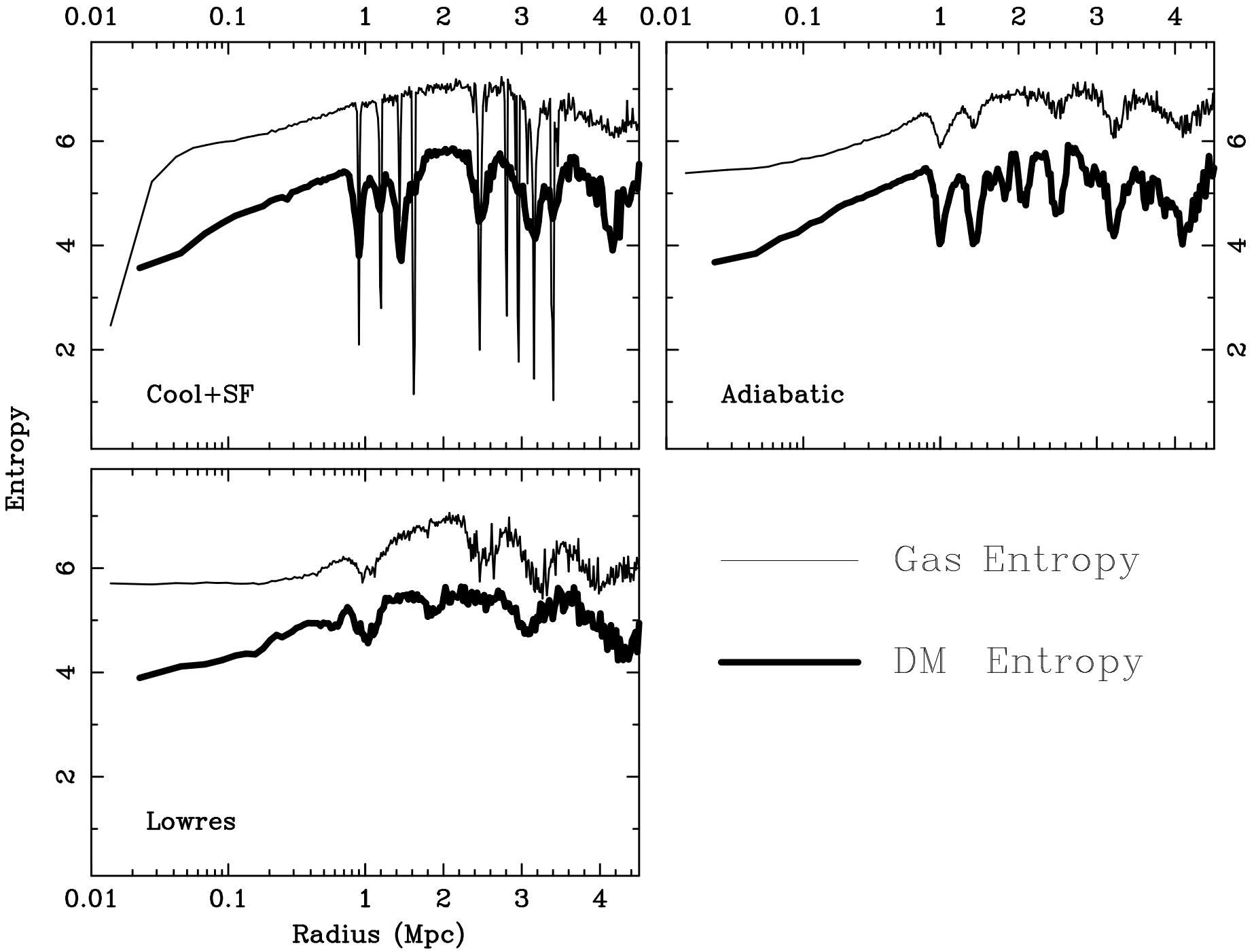
0.01
0.1
1
2
3
4
2
4
6
Entropy
Cool+SF
Adiabatic
Lowres
Radius (Mpc)
Gas Entropy
DM Entropy

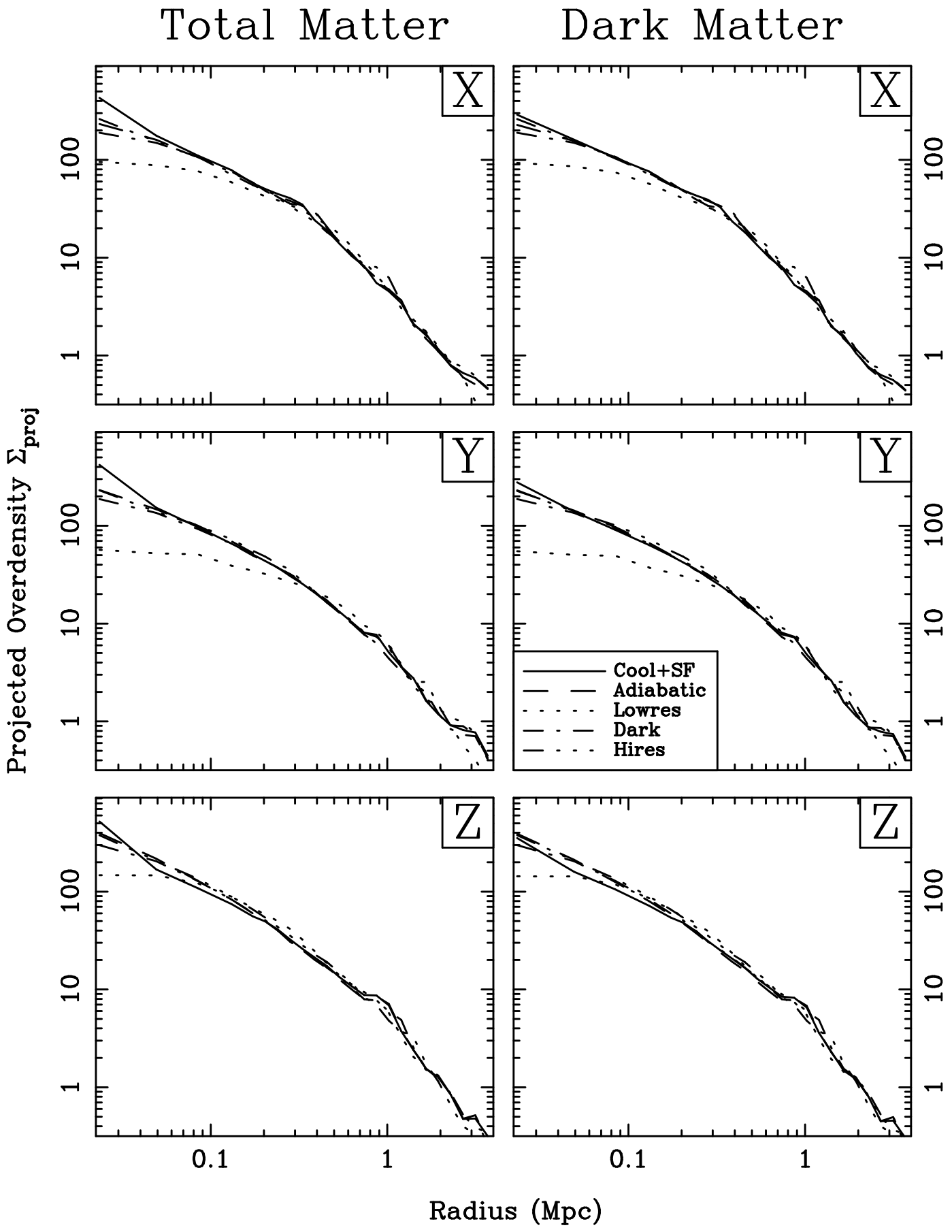
Total Matter
Dark Matter
X
Y
Z
Cool+SF
Adiabatic
Lowres
Dark
Hires
Projected Overdensity Σ_{proj}
Radius (Mpc)
1
10
100
0.1
1

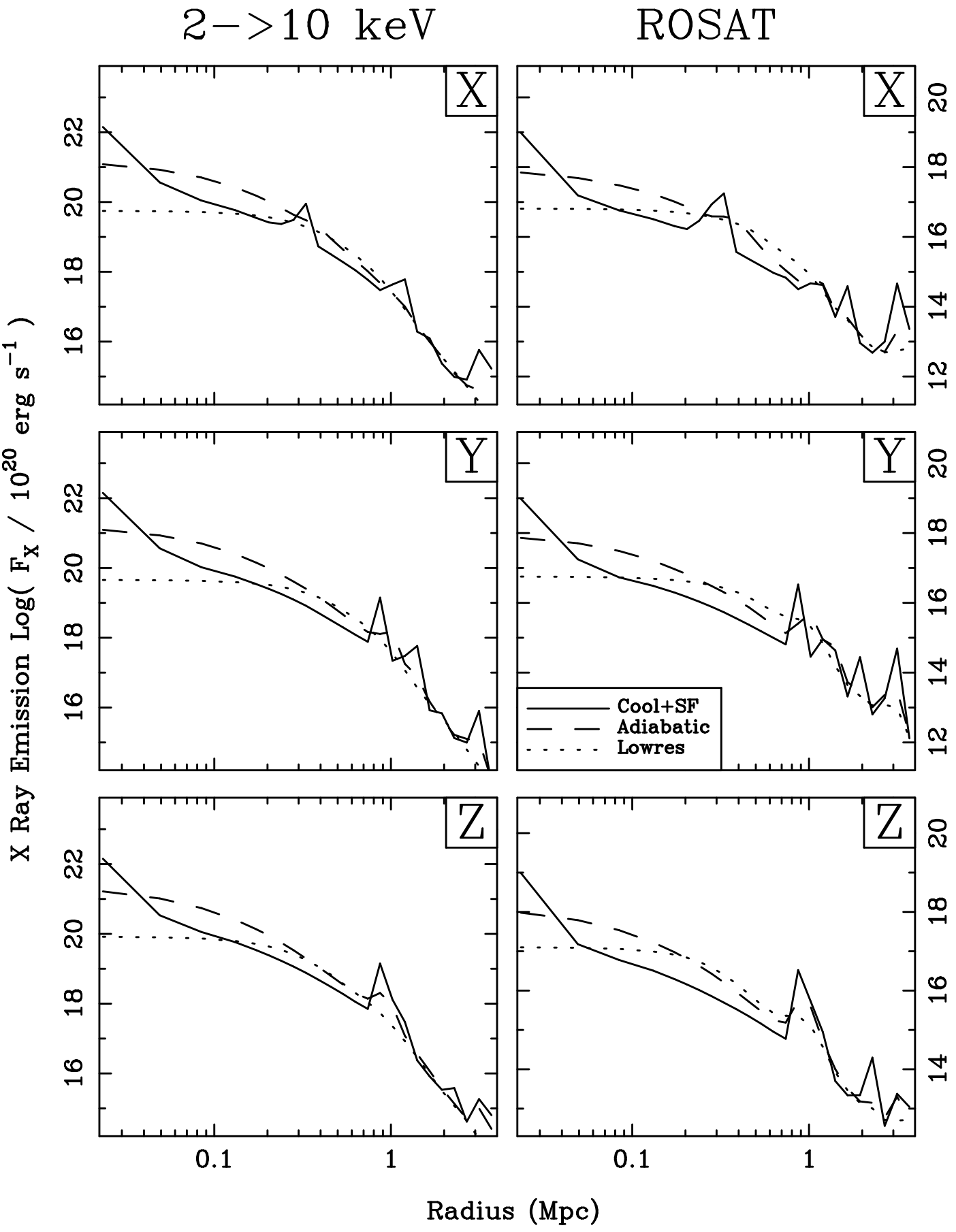
2->10 keV
ROSAT
X
Y
Z
Cool+SF
Adiabatic
Lowres
X Ray Emission Log(F_X / 10^{20} erg s^{-1})
Radius (Mpc)
0.1
1

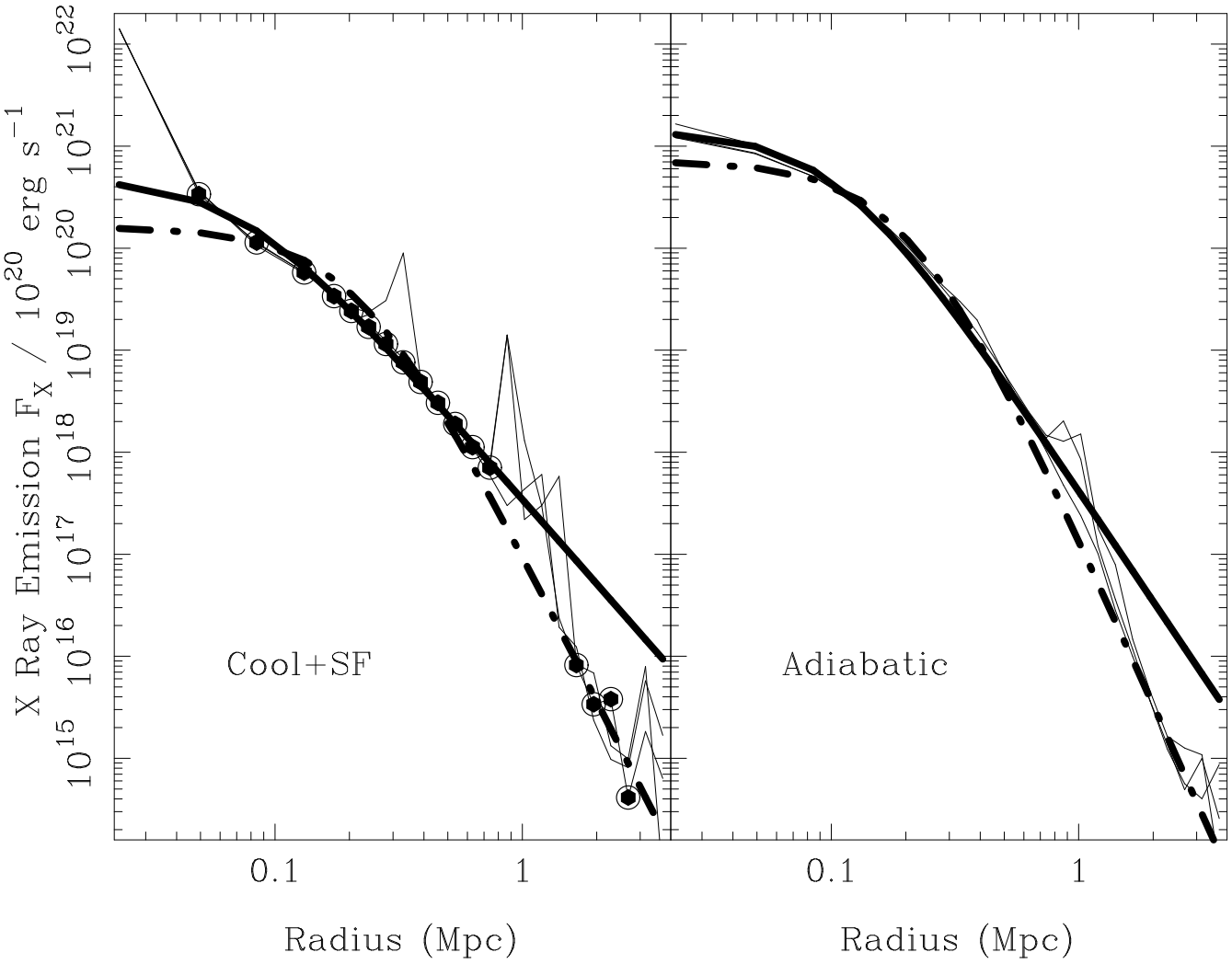
X Ray Emission F_X / 10^{20} erg s^{-1}
10^{15} 10^{16} 10^{17} 10^{18} 10^{19} 10^{20} 10^{21} 10^{22}
Cool+SF
Adiabatic
0.1
1
Radius (Mpc)
0.1
1
Radius (Mpc)

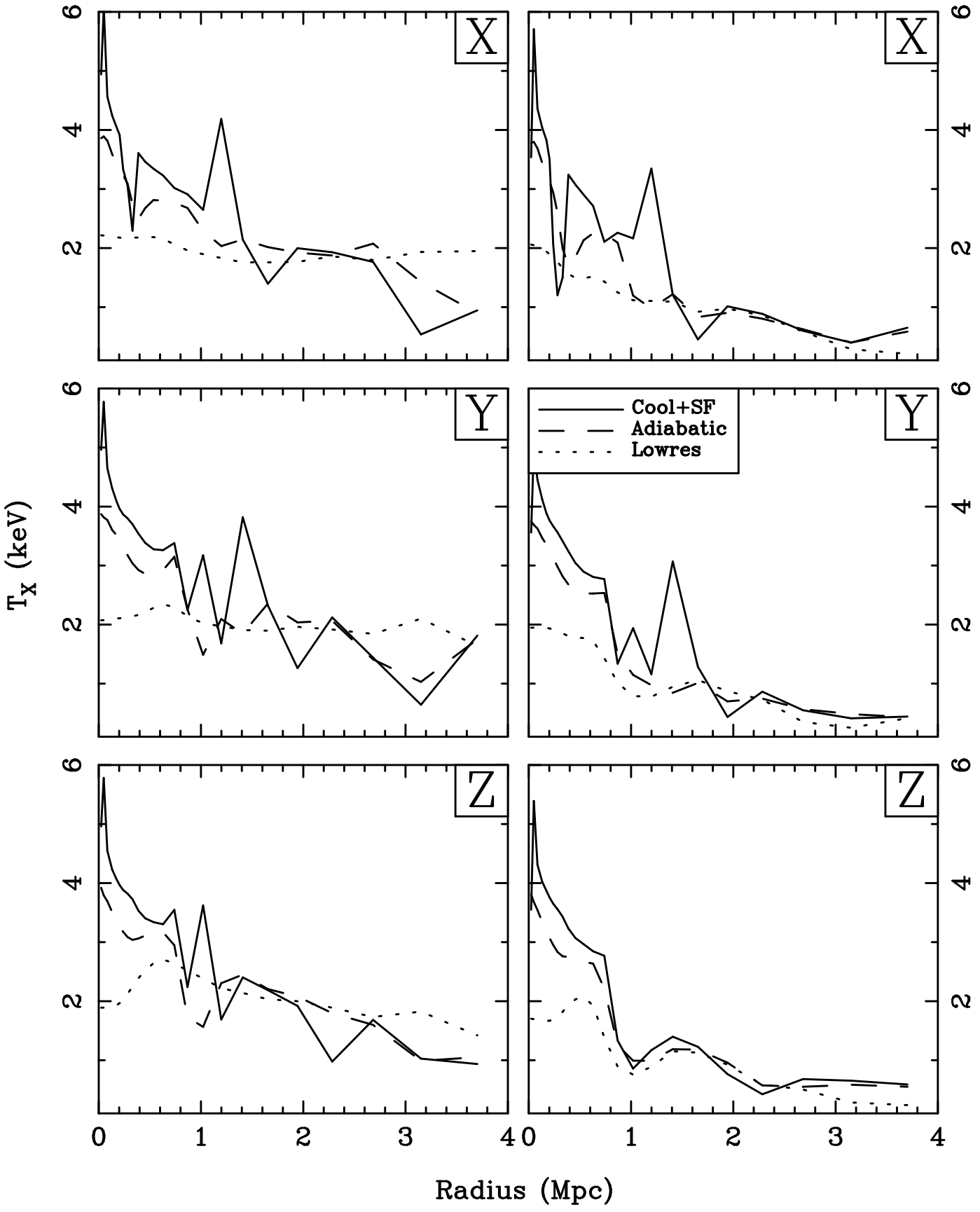
2->10 keV
ROSAT
X
Y
Z
Cool+SF
Adiabatic
Lowres
T_X (keV)
Radius (Mpc)
0
1
2
3
4
2
4
6

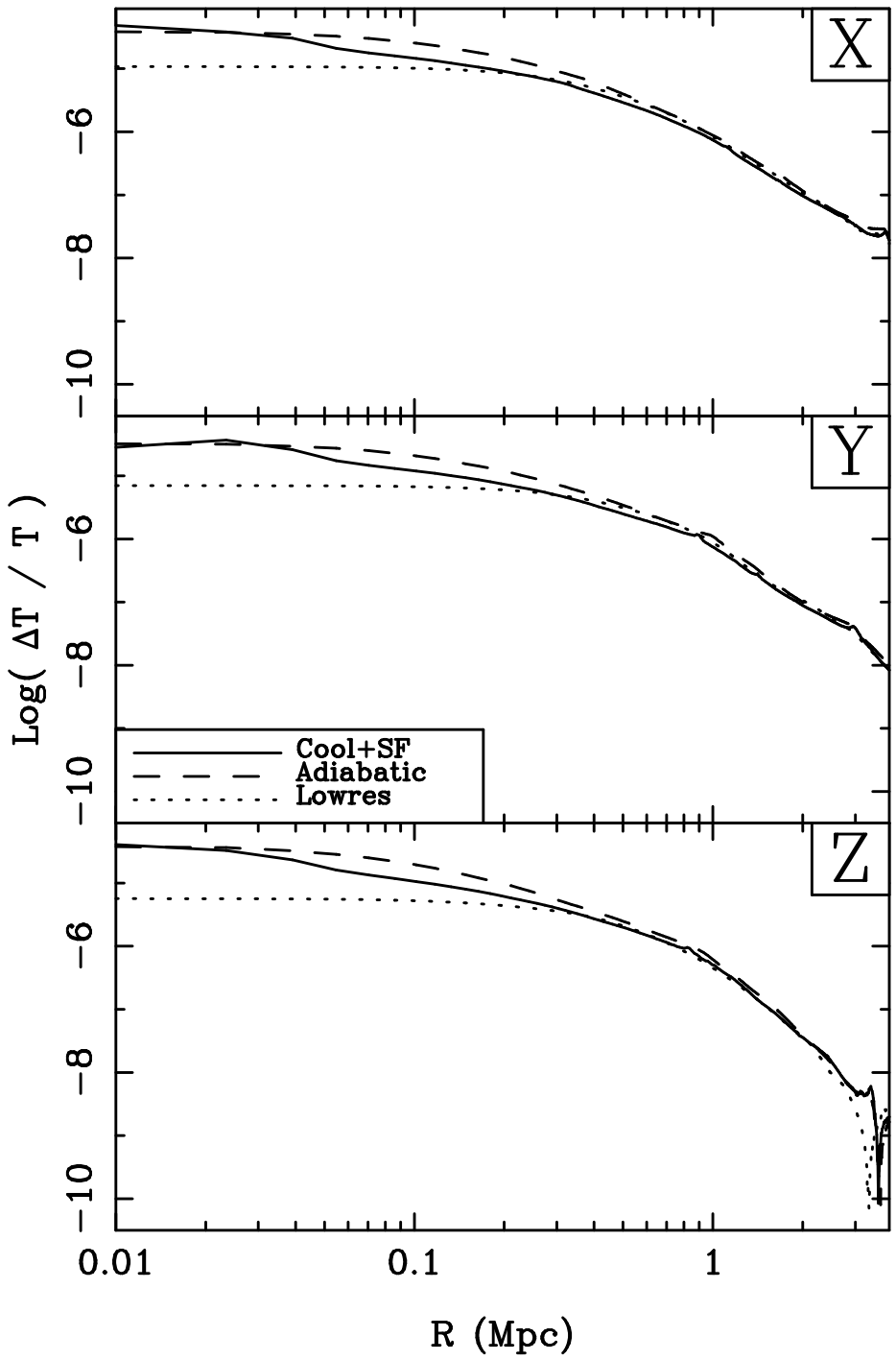
X
Y
Z
Log(ΔT / T)
−6
−8
−10
Cool+SF
Adiabatic
Lowres
0.01
0.1
1
R (Mpc)

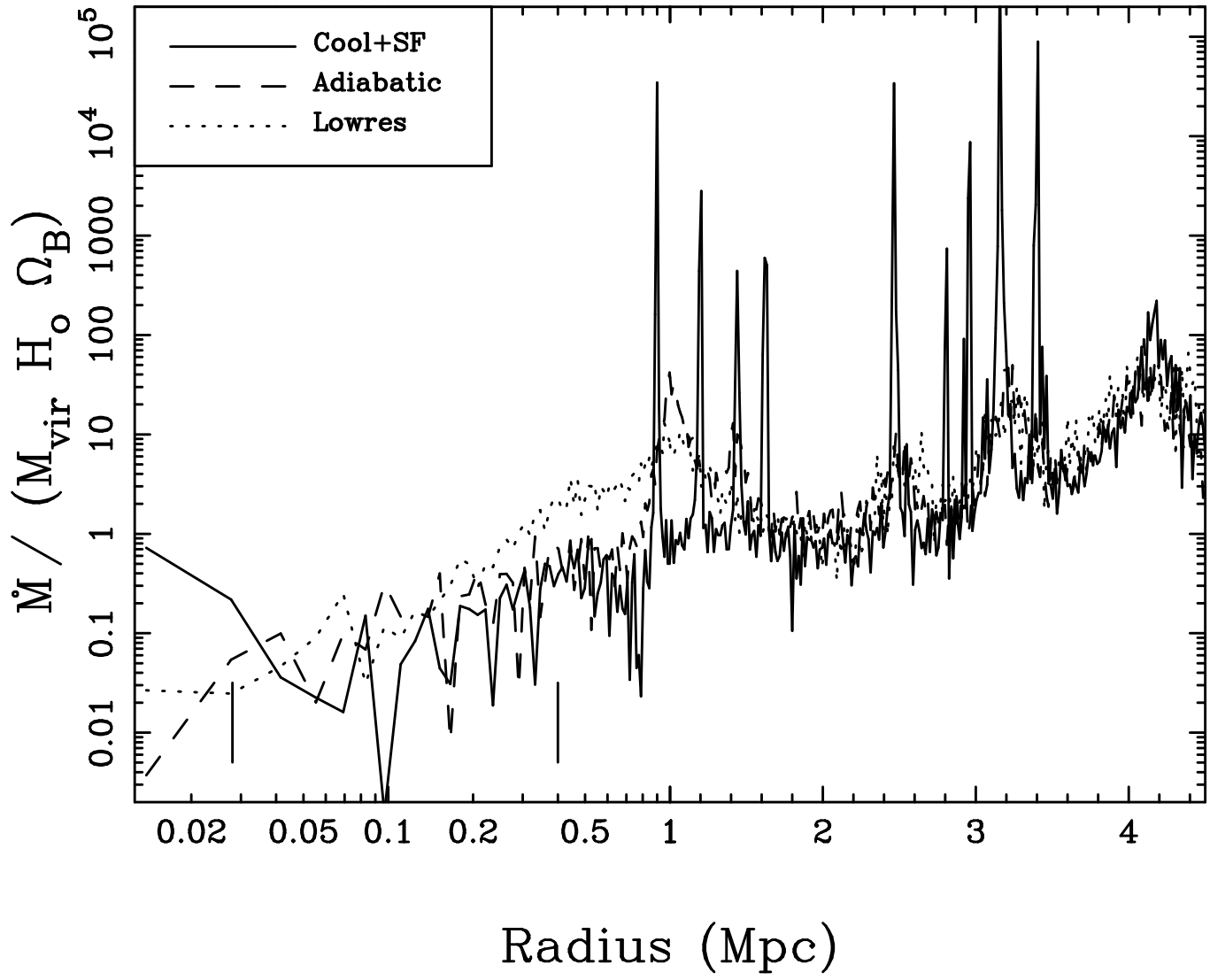
Cool+SF
Adiabatic
Lowres
$\dot{M}$ / (M_{vir} H_o Ω_B)
0.01
0.1
1
10
100
1000
10^4
10^5
0.02
0.05
0.1
0.2
0.5
1
2
3
4
Radius (Mpc)

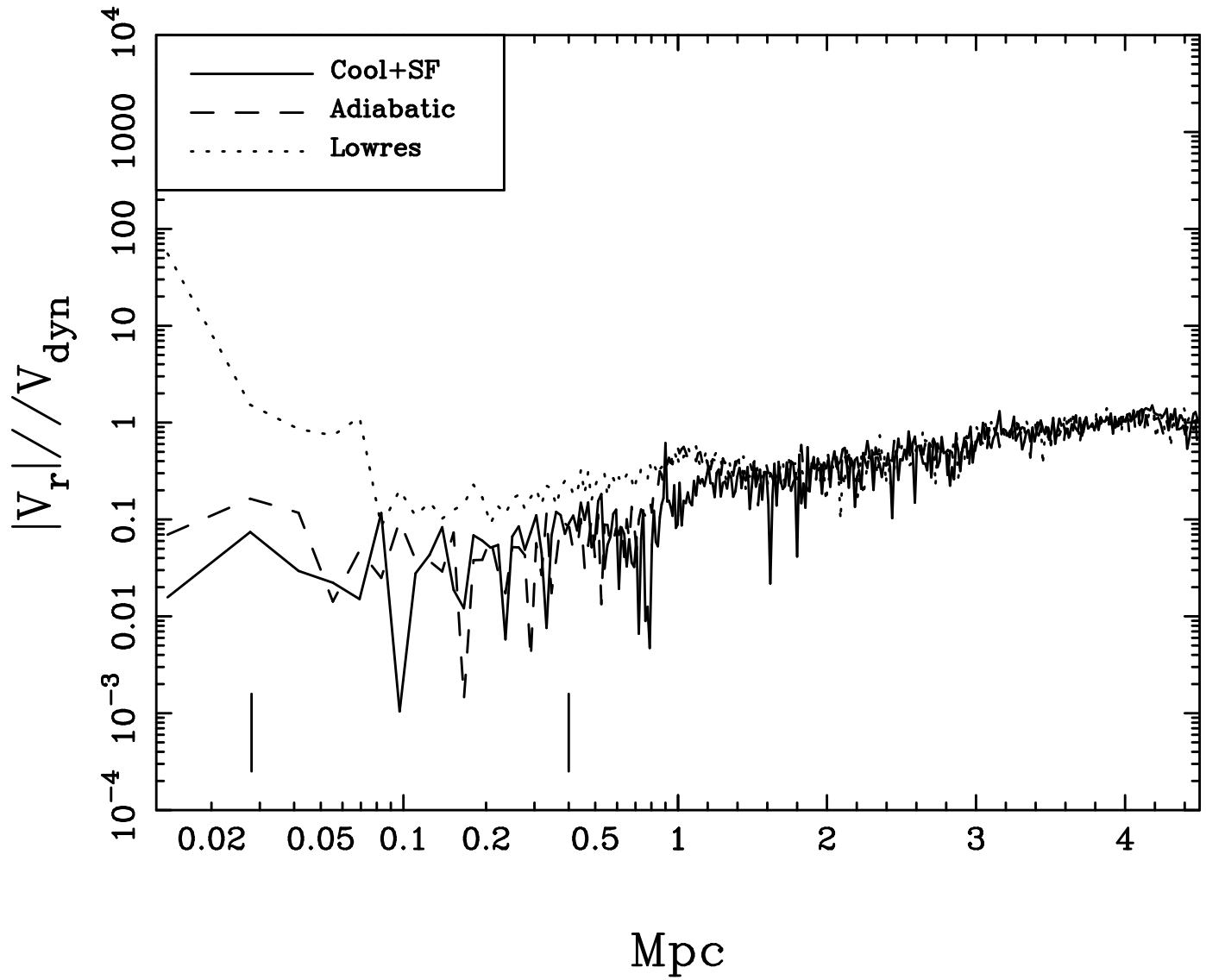
Cool+SF
Adiabatic
Lowres
$|V_r|/V_{dyn}$
10^{-4}
10^{-3}
0.01
0.1
1
10
100
1000
10^4
0.02
0.05
0.1
0.2
0.5
1
2
3
4
Mpc

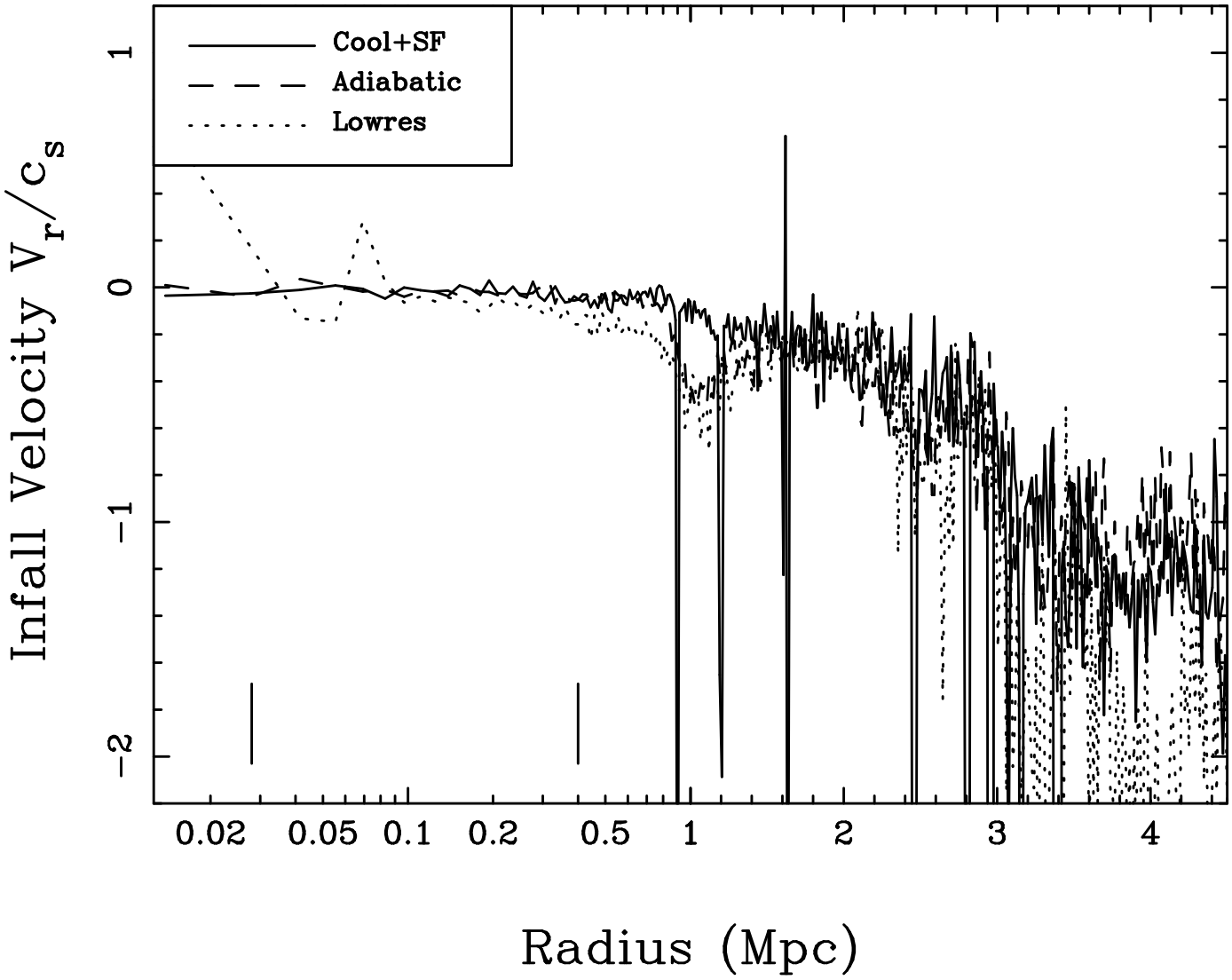
Cool+SF
Adiabatic
Lowres
Infall Velocity V_r/c_s
1
0
−1
−2
0.02
0.05
0.1
0.2
0.5
1
2
3
4
Radius (Mpc)

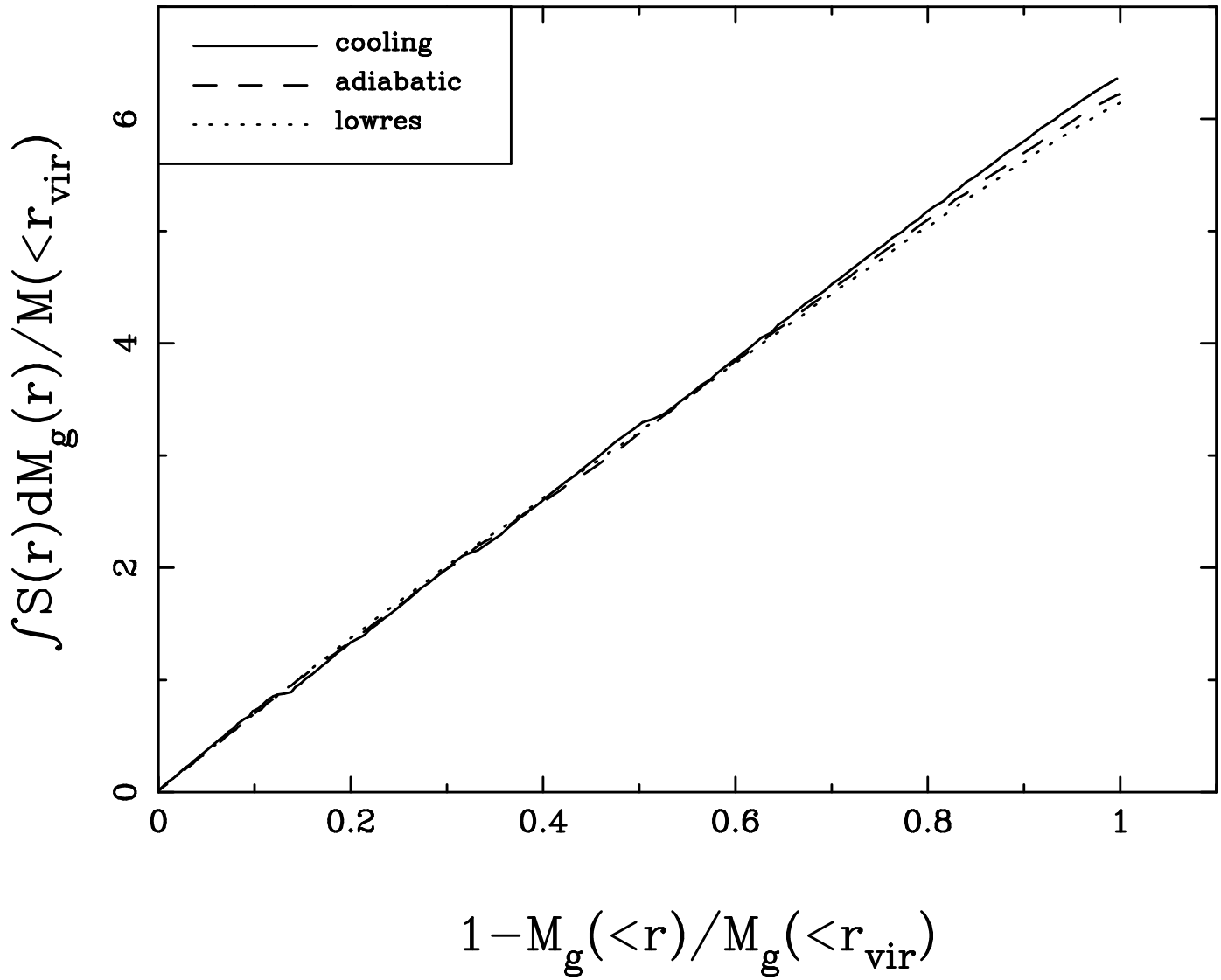
cooling
adiabatic
lowres
0
2
4
6
0
0.2
0.4
0.6
0.8
1
$\int S(r) dM_{g0}(r) / M(<r_{vir})$
$1 - M_g(<r) / M_g(<r_{vir})$